DOKUZ EYLÜL UNIVERSITY
GRADUATE SCHOOL OF NATURAL AND APPLIED SCIENCES

DESIGN OF HIGH FREQUENCY CONTROLLED RECTIFIER FOR A CONTACTLESS BATTERY CHARGING SYSTEM

by
Fahri GÜRBÜZ

October, 2018
İZMİR

DESIGN OF HIGH FREQUENCY CONTROLLED RECTIFIER FOR A CONTACTLESS BATTERY CHARGING SYSTEM

A Thesis Submitted to the
Graduate School of Natural And Applied Sciences of Dokuz Eylül University
In Partial Fulfillment of the Requirements for the Degree of Master of Science in
Electrical and Electronics Engineering Program

by
Fahri GÜRBÜZ

October, 2018
İZMİR

M.Sc. THESIS EXAMINATION RESULT FORM

We have read the thesis entitled **"DESIGN OF HIGH FREQUENCY CONTROLLED RECTIFIER FOR A CONTACLESS BATTERY CHARGING SYSTEM"** completed by **FAHRİ GÜRBÜZ** under supervision of **ASST.PROF.DR. TOLGA SÜRGEVİL** and we certify that in our opinion it is fully adequated, in scope and in quality, as a thesis for the degree of Master of Science.

....

Asst.Prof.Dr.Tolga SÜRGEVİL

Supervisor

....

Prof. Dr. Eyüp AKPINAR — Assoc.Prof. Mutlu BOZTEPE

(Jury Member) — (Jury Member)

Prof.Dr. Kadriye ERTEKIN

Director

Graduate School of Natural and Applied Science

ACKNOWLEDGEMENTS

I would like to express my special appreciation and thanks to my supervisor Asst. Prof. Dr. Tolga SÜRGEVİL. I would like to thank him for encouraging my research.

I would like to acknowledge that this thesis has been carried out as a part of the project "Design and Optimization of a Contactless Charging System for Electric Vehicles" supported by "The Scientific and Technological Research Council of Turkey (TÜBİTAK)" under project grant number 115E116 and I have worked in this project as a scholar. I also would like to thank to Assoc. Prof. Dr. Mutlu BOZTEPE from Ege University and his project group Tuncay DUMAN, Yeliz TEZCAN and Hasret ÜNAL for their help and friendship.

I would like to thank to my family, especially, my mother and father. They have always supported me. Also, I would like to thank to my friends Enes DURBABA and Zekeriya SARI for their guidance during the preperation of this thesis.

Fahri GÜRBÜZ

DESIGN OF HIGH FREQUENCY CONTROLLED RECTIFIER FOR A CONTACTLESS BATTERY CHARGING SYSTEM

ABSTRACT

In this thesis, battery charge current control is aimed in an inductive power transfer system designed for electrical vehicles. Semi-bridgeless active rectifier circuit topology has been used as control circuit on the secondary side. The circuit controls the impedance seen at terminals of secondary side coil controlling the fundamental values of secondary side voltage and current by proper firing signals.

In the study, primary side, secondary side and dual side control types have been investigated and control methods in literature for these types have been mentioned. Operating modes of the active rectifier have been explained and effect of the proposed switching strategy on load have been analysed comparing it with phase shift control. Steady state analysis of the studied system has been made. System performance and optimum load impedance condition have been analysed. Moreover, for both varying frequency and varying load conditions, efficiency, voltage-current gains and input-output power analyses have been made. Also, apparent load under constant input-output voltages and conduction angle have been analysed. In addition, a general coil efficiency comparison among primary, secondary and dual side control methods have been given under different input and output voltages. By that way, advantages and disadvantages of proposed method have been compared with other control types.

Furthermore, losses of switches have been modelled using piecewise linear model and switching and conduction losses have been formulated. Also, calculations have been compared with experimental results. Design steps, control logic and implementation of system have been given in detail. Experimental measurement results of coupling coefficient, timing diagram of the control logic, secondary voltage-current waveforms for resistive and battery load and step responses of closed loop control have been given experimentally. Finally, efficiency comparison of analysis, simulation and experimental results have been given.

Keywords: Inductive power transfer, secondary side control, impedance control, semi-bridgeless active rectifier, battery charging, switching and conduction losses

TEMASSIZ BATARYA ŞARJ SİSTEMİNE YÖNELİK YÜKSEK FREKANSLI KONTROLLÜ DOĞRULTUCU TASARIMI

ÖZ

Bu tezde, elektrikli araçlar için tasarlanan indüktif güç aktarımı sisteminde, şarj akımı kontrolü yapılması amaçlandı. Kontrol devresi olarak ikincil tarafta yarı köprüsüz aktif doğrultucu topolojisi kullanıldı. Devre, ikincil taraftaki sargının uçları arasından görülen yük empedansını, yük voltaj ve akımının temel bileşenini değiştirme yöntemiyle kontrol etmektedir.

Bu çalışmada, birincil, ikincil ve çift taraflı kontrol türleri araştırıldı ve bu kontrol türleri için literatürde bulunan kontrol yöntemlerinden bahsedildi. Aktif doğrultucunun çalışma modları açıklandı. Önerilen anahtarlama yönteminin yük üzerindeki etkisi faz kaydırmalı yöntemle kıyaslamalı olarak verildi. Üzerinde çalışılan sistemin durağan durum analizi yapıldı. Sistem performansı ve en uygun yük koşulu analizleri yapıldı. Ayrıca, hem değişken yük hem de değişken frekans koşullarında verim, giriş-çıkış gücü ve voltaj-akım kazanç analizleri yapıldı. Ayrıca, sabit giriş-çıkış voltaj ve iletim açısı bilgilerine göre yük analizi yapıldı. Farklı giriş-çıkış voltajlarında, birincil, ikincil ve çift taraflı kontrol yöntemleri arasında genel bir sargı verim karşılaştırılması verildi. Bu yolla, önerilen yöntemin avantaj ve dezavantajları diğer kontrol yöntemleriyle karşılaştırıldı.

Buna ek olarak, anahtarların kayıpları parçalı doğrusal model kullanılarak modellendi ve anahtarlama ve iletim kayıpları formülize edildi. Ayrıca, hesaplamalar deneysel sonuçlarla kıyaslandı. Tasarım adımları, kontrol yöntemi ve sistemin uygulanması detaylı olarak verildi. Bağlaşım katsayısı deneysel ölçüm sonuçları, kontrol mantığının zaman diyagramı, rezistif ve batarya yük için ikincil voltaj-akım dalga şekilleri, kapalı çevrimde adım cevapları deneysel olarak verildi. Son olarak, analiz, deney ve benzetim modeli sonuçları karşılaştırılmalı olarak verildi.

Anahtar kelimeler: İndüktif güç aktarımı, ikincil tarafta kontrol, empedans kontrol,

yarı-köprüsüz aktif doğrultucu, batarya şarjı, iletim ve anahtarlama kayıpları

CONTENTS

LIST OF FIGURES

Page

LIST OF TABLES

CHAPTER ONE
INTRODUCTION

Wireless power transfer (WPT) systems have widespread application in biomedical implants, mobile phone or tablet charging and electrical vehicle (EV) charging. They are used in a wide power range from a few milliwatts to a few kilowatts (Kazmierkowski & Moradewicz, 2012). Particularly in the last decade, because of increasing environmental awareness, studies on EVs are focused. However, due to low energy density and long charging time of batteries, EVs' transportation range is quite low. Furthermore, a single charge may take more than one hour which is quite high when compared to gasoline powered vehicles. Hence, EVs cannot become available immediately. In addition, a few hazardous conditions can emerge in cable systems such as any leakage at cable or using in humid environments. WPT systems can eliminate these disadvantages of cable charging systems. Moreover, WPT systems can supply power to EVs whether the vehicle is parked or moving. Hence, power level of battery package can be reduced due to the availability on-line charging systems. Consequently, WPT systems have gained popularity in battery charging systems of them (Li & Mi, 2015).

There are several types of WPT system such as acoustic WPT, light WPT, capacitive WPT and inductive WPT, also known as inductive power transfer (IPT) system. In acoustic WPT systems, electrical power is transferred by a pressure wave through a medium such as air, living tissue or stiff material. In light WPT, laser diodes and photovoltaic diodes are used in the interconversion light and electricity. In capacitive WPT, electrical energy is transferred by means of resonant inverter of which output is connected to two primary metal plates. Applied high frequency power signal is transferred to secondary side metal plates, generating a displacement current between them. IPT systems are operational at high efficiency, at high power applications and in short range. IPT system transfers power in large air gap with primary and secondary side coils coupling magneticaly (Kazmierkowski & Moradewicz, 2012).

In an IPT system, the main elements which take on power transmission task are

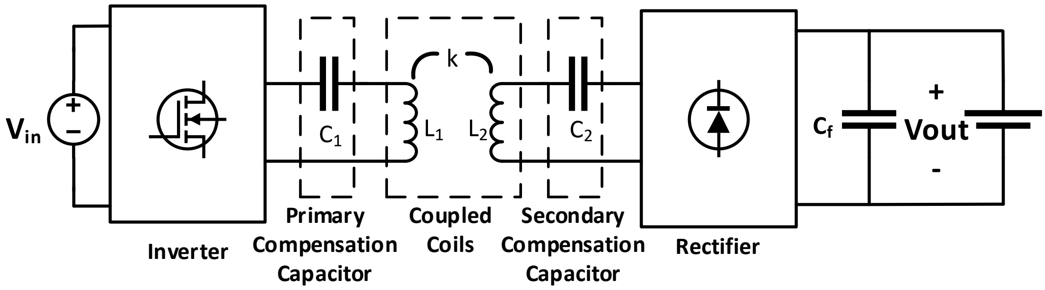

Figure 1.1 Block diagram of series-series compensated IPT system

two resonated coils. There is a rectifier with power factor correction (PFC) circuit to supply dc power at the input of the system. After PFC, there is an inverter circuit which supplies ac voltage to the primary side coil in kHz range at the output of it. The primary side coil is coupled with secondary side coil magnetically through the air. Each coil has a resonance capacitor connected in series or parallel with each other. The resonance capacitors are connected to the circuit so that they interchange the reactive power with the coil inductances in the resonance circuit. Secondary side supplies a rectifier circuit which can be active or passive. Output of rectifier is filtered out by a dc bus capacitor and feeds the battery load. General block diagram of an IPT system is shown in Figure 1.1 (Kazmierkowski & Moradewicz, 2012). There are four types of compensation capacitor circuit for IPT systems. These are series-series (SS), series-parallel (SP), parallel-series (PS) and parallel-parallel (PP). Among these topologies, SS topology is the best topology, since it is less sensitive to load and coupling coefficient variations (Bertoluzzo et al., 2015; Kazmierkowski & Moradewicz, 2012).

Efficiency in IPT systems depends on coupling coefficient variations and loading conditions. The effective load seen by an IPT battery charging system varies with respect to battery charge current. Because of this reason, maximizing the efficiency for all loading conditions in such systems is quite difficult (Bojarski et al., 2014; Bosshard et al., 2014). There are different control methods in literature based on control of battery charge current or making the system run at maximum efficiency point. The control methods can be applied on primary side, secondary side and both sides simultaneously. Dual-side control is based on running the system at maximum efficiency point by properly adjusting the voltage levels on both sides (Bosshard et al., 2014; Diekhans & De Doncker, 2015). Primary side control is based on the control of input power (Chung et al., 2017; Hata et al., 2017) and secondary side control is based on control of apparent impedance seen from output of secondary side coil by means of the controlled rectifier circuit at its terminals (Berger et al., 2015; Colak et al., 2015a,b; Kato et al., 2013; Zhao et al., 2014; Li & Mi, 2015).

In this thesis, a secondary side controlled IPT system is studied. For this purpose, semi-bridgeless active rectifier circuit topology (Colak et al., 2015a) is used so as to reduce the number of switching components. The proposed system is based on resistive switching. In other words, the phase difference between the fundamental waveforms of secondary side voltage and current is set as zero. Switching signals are locked on secondary current phase and resistive switching is aimed. Performance and loss analysis of the proposed control logic are investigated and compared with experimental results.

The chapters of the thesis are organized as follows: The details of the control methods are inspected in Chapter II. Chapter II contains the control types in IPT systems. Advantages and disadvantages of the control methods proposed in the literature are examined and discussed. In the Chapter III, mathematical analysis based on SS compensated topology are performed, proposed secondary side converter topology is investigated. Operating modes of the topology is explained and applicable control methods are examined. Furthermore, effect of the circuit on load impedance is analysed for both purely resistive and phase shift control methods. In Chapter IV, system losses are analysed. The piecewise linear model of the diode and insulated gate bipolar transistors (IGBT) are used in order to make the analysis. In Chapter V, the implementation of secondary side converter and its control are presented. Designed circuits are mentioned and schematic illustrations are given. Moreover, software of the system is explained in details on a flow-chart. Chapter VI consists of experimental and simulation results. The efficiencies of coil, inverter and rectifier circuits are given comparatively. Finally, in Chapter VII, the conclusions are drawn.

CHAPTER TWO

CONTROL METHODS FOR INDUCTIVE POWER TRANSFER SYSTEMS

In IPT systems, efficiency and load matching is vital. Therefore, efficiency or current control at IPT systems becomes more crucial so as to attain a better performance. For this purpose, three different control methods have been developed named as primary side control, secondary side control and dual-side control methods. These three methods are explained in the following subsections.

2.1 Primary Side Control Methods

Primary side control method is based on controlling transferred power to load via controlling primary side voltage and current parameters. This control can be made either using communication with the secondary side or estimating system parameters. Primary side control types are; frequency control based on controlling the switching frequency of inverter, duty control based on the controlling input voltage of the inverter via controlling duty cycle of the dc-dc converter connected to input of the inverter and phase shift control based on controlling phase between PWM signals of inverter legs (Li & Mi, 2015).

In frequency control method, when transferred power is wanted to reduce, operating frequency can be set under or above resonance frequency. In this case, voltage gain decreases as seen from equation (3.21) and this results in decreasing of efficiency. When operating frequency is set below resonance frequency, zero-current switching is made and turn-on loss is apparent. On the other hand, when frequency is carried above resonance value, zero voltage switching is realized and turn-off loss is apparent. However, adding a capacitor across each switch and introducing a sufficient delay to the gate signals significantly reduces the turn-off losses (Erickson & Maksimovic, 2001). Nevertheless, if the system includes bifurcation in power graph as shown in Figure 3.8, in the bandwidth between resonance frequency and higher side peak, system works in capacitive mode. Besides, in the bandwidth between lower side peak and resonance frequency, it works in inductive mode. Thus, if system includes bifurcation, system may not be operated at correct operating frequency in order to achieve ZVS (Boztepe, 2017).

For frequency control, method of Krishan et al. (2012) starts with measuring primary side current. By compiling the current sample with the previous one, it decides whether current has increased or not. The frequency synthesizer generates frequency until current reaches its maximum value. When current is set its maximum value, transferred power is optimal value.

In the study of Chung et al. (2017), researchers have used primary side control method without communication with secondary side. The parameters on which the logic is dependent are inverter input voltage, duty cycle of inverter, switching frequency, coil self inductance and resistance parameters. The proposed logic controls the load voltage. The system calculates input impedance measuring primary side current (fundamental of the primary side voltage is already known because inverter duty cycle is determined). The system estimates load voltage using the estimated values of load resistance and mutual inductance parameters on input impedance. Then, closed-loop controller adjusts the inverter fundamental output voltage by phase shifting of inverter leg PWM signals.

Another primary side control method without communication with secondary side is again based on primary side current measurement (Hata et al., 2017). In this method, in addition to primary side voltage controlling, researchers apply load voltage regulation from secondary side using hysteresis control by running the secondary rectifier in rectification and short modes. Nevertheless, load voltage regulation does not require communication between primary and secondary side. The method simply calculates a reference voltage value for input of the inverter by measuring the primary side current in each mode of the secondary rectifier. Then, input voltage of the inverter is directly controlled to operate the system in maximum efficiency point.

2.2 Secondary Side Control Methods

Secondary side control method is based on control of output power via control of secondary side parameters. Secondary side control methods are applied on an active rectifier or dc-dc converter cascaded with diode rectifier without any communication with primary side. Because secondary side control parameters which can be charge current, maximum efficiency point or phase difference between secondary side voltage and current are on the same side with the controller. Both duty and phase shift control is available in secondary side control method. Furthermore, these two control methods can be used combining them. The general logic behind of the secondary side control method is to adjust the impedance seen from input terminal of rectifier. For this purpose, influence of different kind of dc-dc converters and methods on the load is examined below.

One of the dc-dc converter topologies as impedance matching circuit is buck converter (Kato et al., 2013). The converter is cascaded with a diode rectifier on secondary side. At this study, researchers are first analysed effect of the load on efficiency. After that, the effect of duty cycle on load is investigated at buck converter topology and this effect is formulated as;

$$Z_{in} = \frac{R_L}{D^2} \tag{2.1}$$

where Z_{in}, R_L and D are input impedance seen from buck converter terminals, load at output of the converter and duty cycle of the converter, respectively. As seen from equation (2.1), the apparent dc load is changed from infinite to R_L.

Another impedance matching topology is cascaded diode rectifier, buck and boost converters, respectively (Colak et al., 2015b). In the buck operation; input voltage is higher than load voltage and in the boost operation; input voltage is lower than load voltage value. The aim of this topology is to control apparent load in a large range. Hence, impedance variation in this topology is between zero and infinitive value. Also, relation between rectifier input voltage (V_2) and dc output voltage (V_o) is shown as follows;

$$\frac{|V_S|}{V_o} = \frac{1 - D_{S2}}{D_{S1}} \tag{2.2}$$

where D_{S1} and D_{S2} are duty cycle ratio of buck and boost converter, respectively. Control logic starts with sampling of secondary side voltage and current. Input impedance is calculated on sampled voltage-current values and compared with reference impedance value. Closed loop control maintains constant resistor at the diode rectifier output.

In the study of Colak et al. (2015a), secondary side control circuit topology is designed as semi bridgeless rectifier which consists of two switches and diodes placed lower side, diodes are anti-parallel component of the switches and two diodes placed upper side of the circuit. These two switches are controlled with two different PWM signals which have phase according to each other. The purposed control method is based on shifting the phase between these PWM signals. As a result of phase shifting, conduction angle, real and imaginary parts of the load are changed. Effect of switching strategy is formulated in equation (3.8) for inductive control and equation (3.10) for capacitive control.

For the secondary side control, both amplitude and phase shift control are possible by using full bridge active rectifier cascaded by a buck converter (Berger et al., 2015). In this study, researchers propose two control parameters. One of them is phase angle between fundamentals of secondary side voltage and current. The other one is conduction angle in order to control charge current. Conduction angle can be controlled using either active rectifier or dc-dc converter. Combining control of these two parameters provides the control of both magnitude and phase angle of the apparent load. Impedance expression is shown as follows;

$$Z_L = \frac{V_L}{I_L} = \frac{4}{\pi}\frac{V_r}{I_L}e^{-j\phi} \tag{2.3}$$

where Z_L, V_L, I_L, V_r and ϕ are secondary side apparent load, fundamental values of secondary side voltage-current, rectifier output voltage and phase angle between fundamentals of secondary side voltage and current, respectively. When dc-dc converter is run, full bridge active rectifier is responsible from controlling the phase angle and rectifying secondary voltage and current. Controlling amplitude of voltage is made by a dc-dc converted cascaded with the active rectifier. The aim of the control is to adjust real and imaginary parts of the load impedance independently.

Another secondary side control method does not use a compensation capacitor on the secondary side, whereas primary side has compensation capacitor (Zhao et al., 2014). In addition to that, secondary side circuit is an active rectifier. In order to control reactive power, full bridge active rectifier is used as bidirectional circuit. Phase angle between primary and secondary side voltages varies from 0 to 180^0 and determines transferred power to the load. Thus, control strategy is based on controlling the phase angle between primary and secondary voltages. The transferred power expression is given as follows;

$$P_S = \frac{8}{\pi^2}\frac{V_S V_P}{\omega M}\sin(\phi) \tag{2.4}$$

where P_s, V_s, V_p, ϕ, ω and M are transferred power to secondary side, secondary voltage, primary voltage, phase angle between primary and secondary voltages and mutual inductance, respectively. As seen from equation (2.4), maximum power transfer is realized at 90^0.

2.3 Dual-Side Control Methods

Dual-side control method is the most effective method in the control strategies. It is applied on both primary and secondary side. Dual-side control advantages and disadvantages are given as follow;

- Communication is a must. At dual-side control strategy, according to secondary side controlled parameters, primary side applies its control output to system.
- Because of the communication and microcontroller need in the both side, dual-side control is the most expensive method in control methods.
- Efficiency can be optimised.

- Dual-side control is more complicated than secondary side and primary side control methods.

In the study of Diekhans & De Doncker (2015), a dual-side control method is purposed. The method is based on running the system at nominal voltage ratio. Secondary side control circuit is designed as semi-bridgeless active rectifier (switches are placed at lower side of the circuit). This circuit applies a control method so that apparent load is resistive. In other words, controller warrants that there is not phase angle between fundamental of secondary side voltage and current. However, the applied conduction angle (β) makes a change at fundamental of secondary voltage. Secondary voltage and conduction angle is sent to primary side microcontroller via wireless communication. According to ratio between non-switched primary and secondary voltages, another conduction angle (α) is calculated and applied to primary side voltage on inverter. Here, it is understood that, α and β angles have an impact on output power and its expression is given as follows;

$$P_{out} = \frac{8}{\pi^2}\frac{V_{1,DC}V_{2,DC}}{\omega M}\sin\left(\frac{\alpha}{2}\right)\sin\left(\frac{\beta}{2}\right) \tag{2.5}$$

In the control scheme, secondary side PI controller generates a β and transfers it to primary side together with secondary side dc voltage value. Primary side calculates conduction angle α for inverter circuit using the following equation:

$$\frac{V_{1,DC}}{V_{1,DC,N}}\sin\left(\frac{\alpha}{2}\right) = \frac{V_{2,DC}}{V_{2,DC,N}}\sin\left(\frac{\beta}{2}\right) \tag{2.6}$$

where α and β are primary and secondary side conduction angle, $V_{1,DC}$, $V_{1,DC,N}$, $V_{2,DC}$, $V_{2,DC,N}$ are primary side inverter input voltage value, primary side inverter input voltage nominal value, secondary side inverter input voltage value and secondary side inverter input voltage nominal value, respectively.

Another dual-side control is examined in the study of Geng et al. (2016). Secondary side control circuit is designed as a diode rectifier and cascaded buck converter. As before mentioned, the control logic begins on secondary side. The secondary side control logic estimates duty cycle and applies for buck converter according to following equation.

$$D = \sqrt{\frac{8}{\pi^2 R_{eq\_opr\_\eta}} \frac{U_{sc}}{I_{sc}}} \tag{2.7}$$

where $R_{eq\_opr\_\eta}$ is apparent load value seen from diode rectifier at optimal efficiency condition, U_{sc} and I_{sc} are voltage and current value of the dc output, respectively. The charge current value is sent to primary side on wireless communication. According to error value between reference and actual values of the charge current, PI controller generates a conduction angle for primary side inverter circuit in order to adjust the fundamental input voltage.

The next strategy uses a reference value calculation for primary side control (Bosshard et al., 2014). Secondary side control circuit is designed as cascaded diode rectifier and boost converter. At secondary side control, battery power is calculated with respect to reference charge current. Afterwards, using the following equation, reference value of secondary side voltage is calculated.

$$U_2^* = \sqrt{\frac{\pi^2}{8} \omega_o L_2 k P_2} \tag{2.8}$$

where U_2^*, L_2, ω_o, k and P_2 are reference value of secondary side voltage, secondary side inductance value, operating frequency, coupling coefficient between coils and output power, respectively. Using U_2^* and the following equation, reference value of primary side voltage U_1^* is calculated and sent to primary side control circuit and applied.

$$U_2^* = \sqrt{\frac{L_1}{L_2}} U_{2,dc}^* \tag{2.9}$$

where L_1 is primary side inductance value. Afterwards, using U_2^*, reference value of input current of boost converter I_b^* is calculated by PI controller. According to I_b^*, the PI controller generates PWM pulses for boost converter.

CHAPTER THREE

THEORETICAL ANALYSIS OF IPT SYSTEM WITH SECONDARY SIDE ACTIVE RECTIFIER

The general view of the series-series (S-S) compensated IPT system topology is illustrated in Figure 3.1. In this system, DC input voltage V_{in} is switched using full-bridge inverter at the angular frequency of $\omega = 2\pi f$. As a result, square wave voltage is applied to primary side resonance circuit. The function of the secondary-side active rectifier circuit is to provide adjustable dc charge current to the battery. It consists of two switches named as S_7, S_8 placed on the lower side of the circuit and four fast recovery diodes two of which are placed on the upper side of the circuit (D_5, D_6) and the other two diodes (D_7, D_8) are placed on the lower side of the circuit as anti-parallel diodes of semiconductor switches. Input of the circuit is connected to the secondary side coil. The output is connected to a dc bus capacitor which feeds the battery as load.

Secondary-side active rectifier circuit limits the charge current by triggering S_7 and S_8 switches and shorting the output of the secondary side coil during a certain time interval. The switching methods that can be applied with this topology are purely resistive control and phase shift control. These are explained in the following subsection.

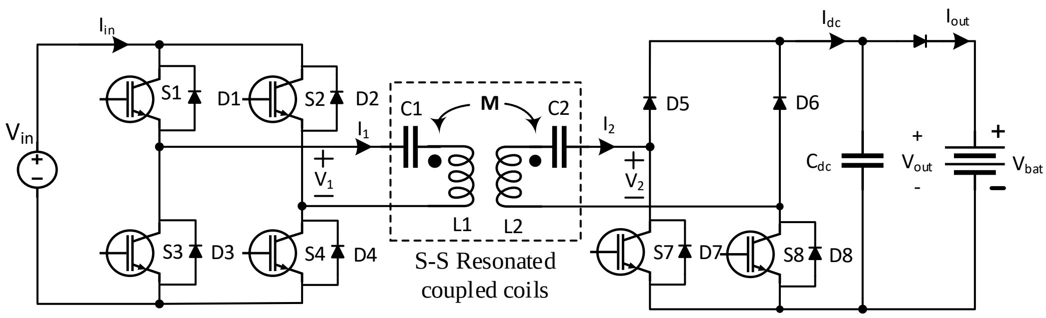

Figure 3.1 General view of a series-series compensated IPT system

3.1 Operating Modes of Secondary-Side Active Rectifier

This circuit has four operating modes. These modes are illustrated in Figure 3.2 for possible switching states and explained below (Colak et al., 2015a). The battery is represented by an equivalent dc resistor, R_{dc}. The semiconductor devices are assumed to be ideal.

Mode - 1: In this mode, the secondary side current polarity is positive. In this condition, the switch S_7 is triggered and current turns back to source through S_7 switch and D_8 diode. As seen in Figure 3.2(a), the source does not feed the load. The dc bus capacitor feeds the load and V_2=0.

Mode - 2: In this mode, the switches are not triggered. The current follows the path which is formed by D_5 and D_8 diodes. The source feeds the load and dc bus capacitor and V_2 = V_{out}. Current path of this mode is illustrated in Figure 3.2(b).

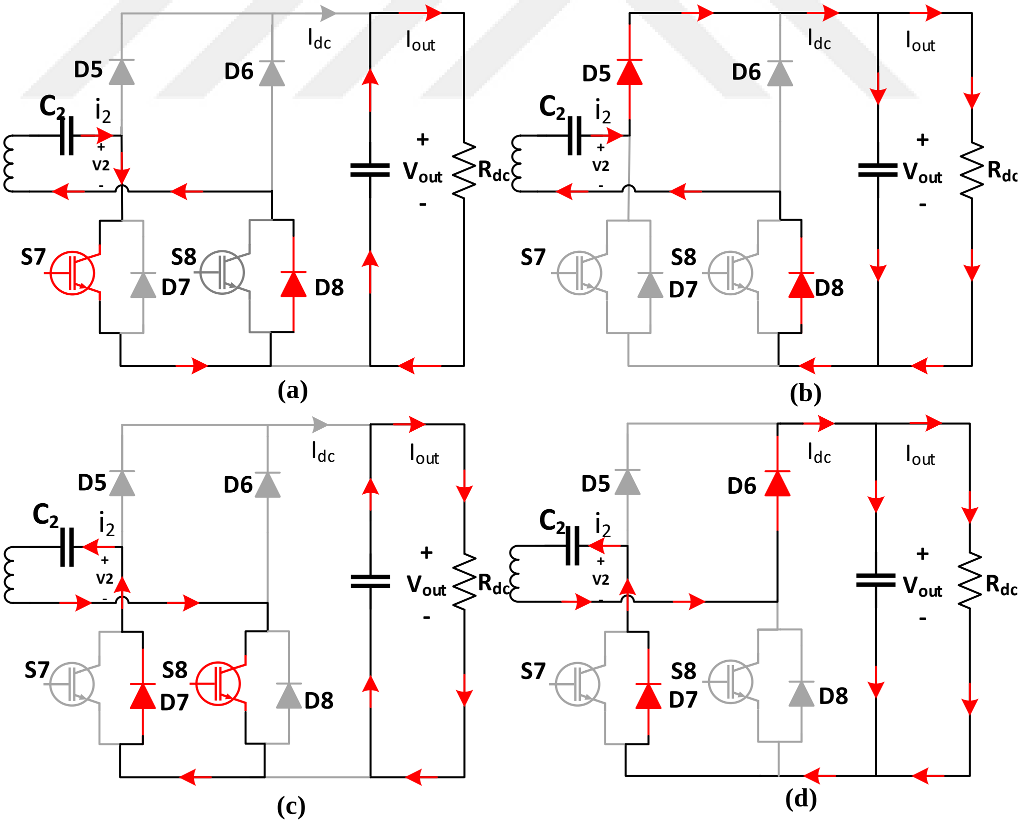

Figure 3.2 Operating modes of secondary-side active rectifier circuit

Mode - 3: In this mode, the secondary current polarity is negative. S_8 switch must be triggered. The current complete the circuit through S_8 switch and D_7 diode. Likewise Mode - 1, current does not feed the load in Mode - 3. The secondary side coil is shorted V_2=0. Moreover, dc bus capacitor feeds the load. This mode is shown in Figure 3.2 (c).

Mode – 4: In this mode, the polarity of the current is still negative and it is similar to Mode – 2. The source feeds the load and dc bus capacitor $V_2 = V_{out}$. The current follows the path which is formed by D_6 and D_7 diodes. This mode is illustrated in Figure 3.2(d).

3.2 Control Methods for Secondary-Side Active Rectifier

The first applicable control method is purely resistive control. In this strategy, rectifier is allowed to feed load at a conduction angle value (β) that is symmetrically placed between two zero-crossing points of secondary side current. As a result, the fundamental components of secondary side current and voltage are in phase. This control method is illustrated in Figure 3.3 (a). When switches are not triggered, the current goes through diodes (D_5-D_8 for positive cycle, D_6-D_7 for negative cycle) throughout conduction angle, which is between $(\pi-\beta)/2$ and $(\pi+\beta)/2$ as shown in Figure 3.3 (a).

Another switching strategy which can be applied is phase shift control. In this strategy, there are two different switching methods which are inductive control and

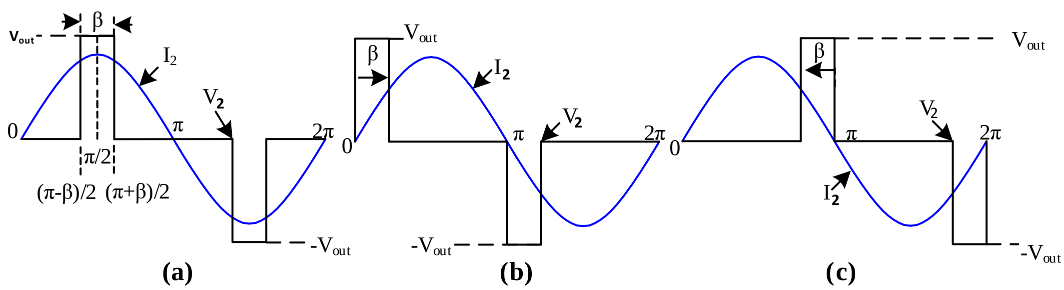

Figure 3.3 Switching methods a) purely resistive control b) inductive control c) capacitive control

capacitive control. Inductive control is applied when secondary side current changes its polarity from negative to positive. In that condition, conduction angle grows from 0 to π. In addition to that, fundamental component of the secondary side voltage leads to secondary side current. This control method is shown in Figure 3.3 (b) (Colak et al., 2015a). The other condition for pure phase shift control is capacitive control shown in Figure 3.3 (c). Capacitive control is applied when current changes its polarity from positive cycle to negative cycle. At capacitive control, conduction angle grows from π to 0. In this control type, secondary side current leads to fundamental component of the secondary side voltage (Colak et al., 2015a).

3.3 Load Analysis According to Switching Strategy

According to switching strategy, reactive power may be circulated in the circuit or the circuit is run in resistive load condition. The apparent load seen from output of the secondary side coil may be purely resistive or a load having both real and reactive part. This situation affects the analysis of the system because of the apparent load type, since load type and conduction angle β affects the real and reactive power and output power. Particularly, in phase-shift control, the apparent load has a large reactive part in low conduction angle values while it has large real part when conduction angle increases.

When the circuit is run in resistive mode, the fundamental secondary side voltage expression obtained from Fourier series expression is;

$$V_{2,peak} = \frac{4}{\pi} V_{out} \sin\left(\frac{\beta}{2}\right) \sin(\omega t) \tag{3.1}$$

and fundamental value of secondary side current is;

$$I_{2,peak} = \frac{\frac{\pi}{2} I_{out}}{\sin\left(\frac{\beta}{2}\right)} \sin(\omega t) \tag{3.2}$$

where I_{out} and V_{out} are load current and voltage as shown in Figure 3.2, respectively. The ratio of the equations (3.1) and (3.2) is equal to apparent load resistor of the rectifier input and is written as follows;

$$R_L = \frac{V_{2,peak}}{I_{2,peak}} = \frac{8}{\pi^2} \left(\sin\left(\frac{\beta}{2}\right)\right)^2 R_{dc} \tag{3.3}$$

where $R_{dc} = V_{out} / I_{out}$ is the dc load resistor.

As seen from equation (3.3), conduction angle has effect on the load with square of the sine function. Figure 3.4 shows the variation of the load with respect to conduction angle.

In order to calculate phase-shift control load condition, first, average value of the switched current, in other words, average value of the rectifier output current before the capacitor (I_{dc}) must be calculated. According to Figure 3.3 (b) and 3.3 (c);

$$I_{out} = \frac{1}{\pi}\int_0^{\beta} I_{2,peak}\sin(\theta)\,d\theta \tag{3.4}$$

From here, average value of the current that is across the load is;

$$I_{out} = I_{2,peak}\frac{1-\cos(\beta)}{\pi} \tag{3.5}$$

From equation (3.5), peak value of secondar current is written as follows;

$$I_{2,peak} = I_{out}\frac{\pi}{1-\cos(\beta)} \tag{3.6}$$

According to Figure 3.3 (b), the voltage equation for inductive mode is;

$$V_{2,peak} = \frac{4}{\pi}V_{out}\sin\left(\frac{\beta}{2}\right)e^{j\left(\frac{\pi}{2}-\frac{\beta}{2}\right)} \tag{3.7}$$

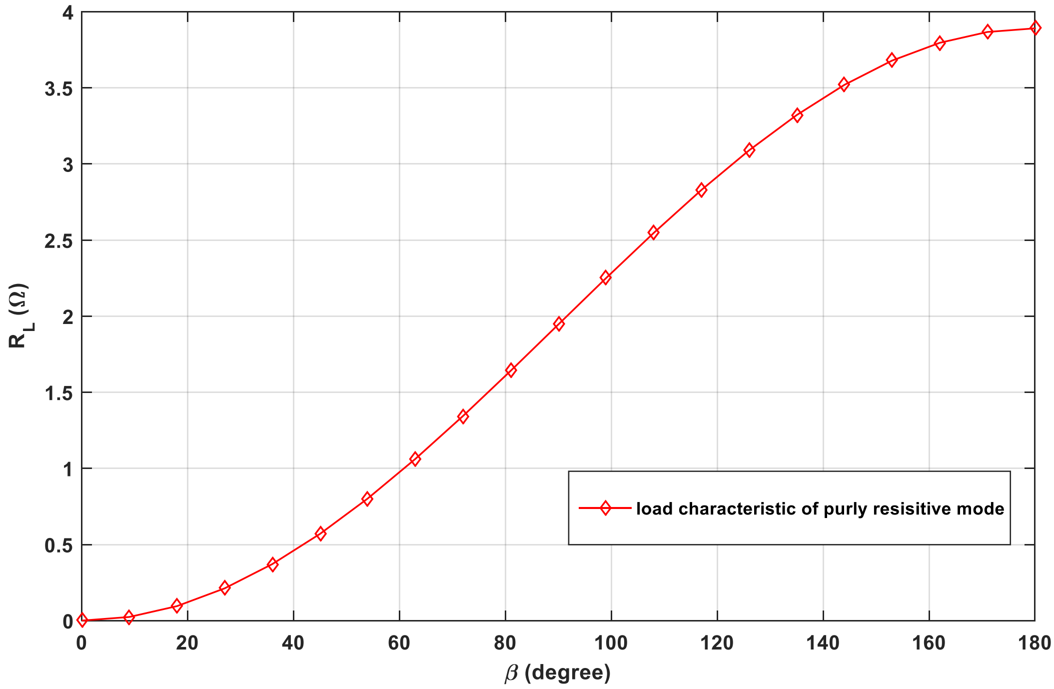

Figure 3.4 Change of load with respect to β for purely resistive control (R_{dc}=4.8 Ω)

On this condition, the load equation is (Colak et al., 2015a);

$$Z_L = \frac{V_{2,peak}}{I_{2,peak}} = \frac{4}{\pi^2}(1-\cos(\beta))\sin\left(\frac{\beta}{2}\right)R_{dc}e^{j\left(\frac{\pi}{2}-\frac{\beta}{2}\right)} \tag{3.8}$$

The capacitive mode voltage and load formulae are shown as follows (Colak et al., 2015a);

$$V_{2,peak} = \frac{4}{\pi}V_{out}\sin\left(\frac{\beta}{2}\right)e^{j\left(\frac{\beta}{2}-\frac{\pi}{2}\right)} \tag{3.9}$$

$$Z_L = \frac{V_{2,peak}}{I_{2,peak}} = \frac{4}{\pi^2}(1-\cos(\beta))\sin\left(\frac{\beta}{2}\right)R_{dc}e^{j\left(\frac{\beta}{2}-\frac{\pi}{2}\right)} \tag{3.10}$$

As it is seen from equation (3.8) and (3.10), load characteristics are quite similar except their angle. Thus, on condition that β interval is defined as $0 \leq \beta \leq \pi$, equations (3.8) and (3.10) can be used to represent both operating condition. Figure 3.5 (a) and 3.5 (b) shows variation on the load with respect to β value at inductive and capacitive switching, respectively.

3.4 Steady State Analysis

The equivalent circuit for the primary and the secondary side coils is a loosely coupled transformer model which is shown in Figure 3.6 (Bertoluzzo et al., 2015; Bojarski et al., 2014). In the steady state analyses, the fundamental harmonic approach is used. In the equivalent circuit, V_1 is the fundamental component of the output voltage of the inverter at the switching frequency. L_1 is the primary, L_2 is secondary side coil self-inductances and M is mutual inductance between the coils. C_1, C_2 are primary and secondary side compensation capacitors, respectively. R_1 and R_2 are the parasitic resistors of the primary and the secondary side coils. Z_{in} is the apparent input impedance from primary side coil input terminals. The apparent load at the input of secondary side rectifier is shown by Z_L which has real and reactive parts.

The analysis of the system is investigated by applying Kirchhoff Voltage Law (KVL) on the equivalent circuit illustrated in Figure 3.6. If the load is assumed to have both real and reactive part, (*i.e.* $Z_L = R_L + jx_L$) the primary and secondary side impedances

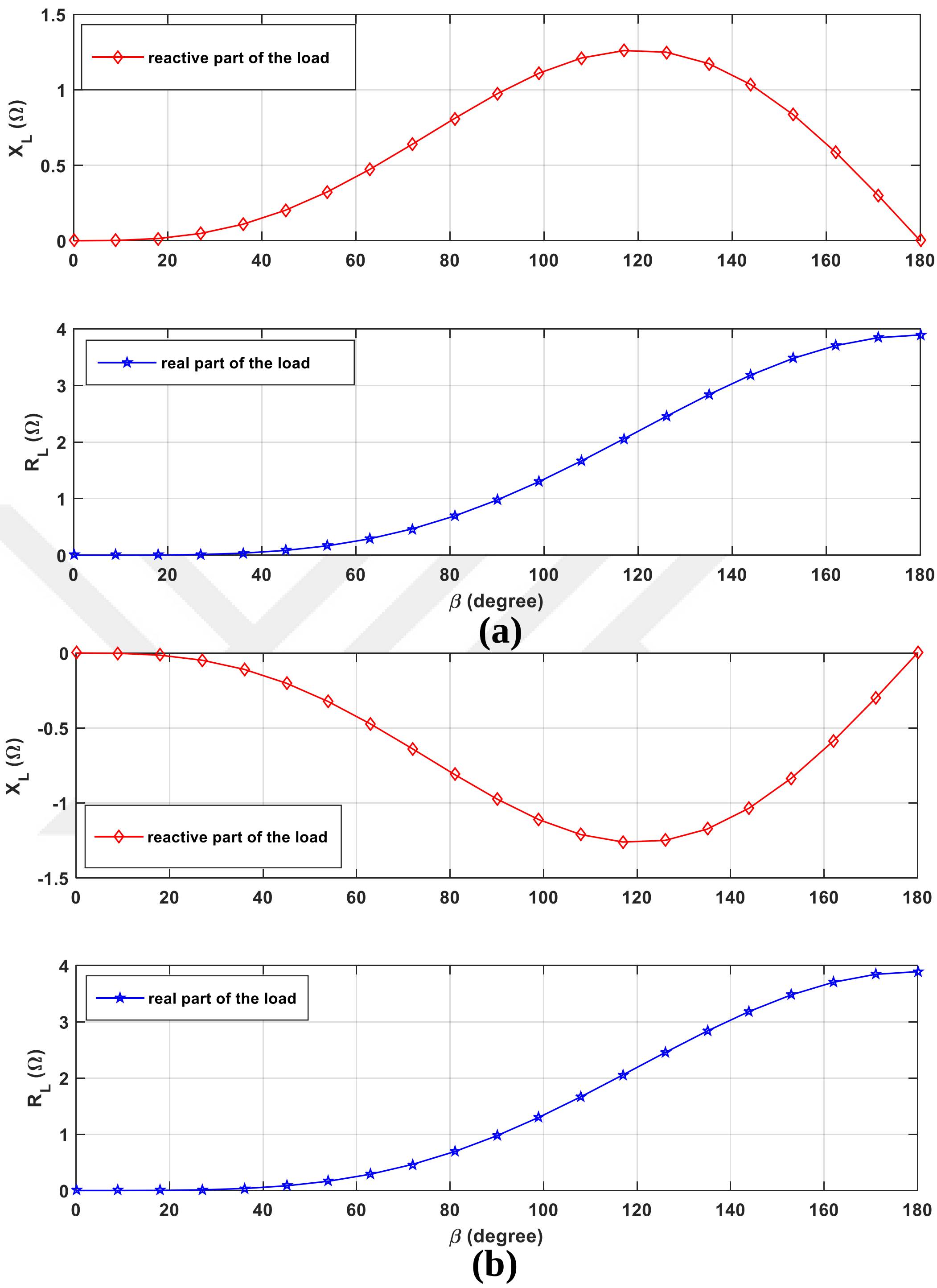

Figure 3.5 Change of real and reactive part of the apparent load with respect to β a) inductive control b) capacitive control (R_{dc}=4.8 Ω)

are defined as follows;

$$z_1 = R_1 + jx_1 \tag{3.11}$$

$$z_2 = R_2 + R_L + jx_2 \tag{3.12}$$

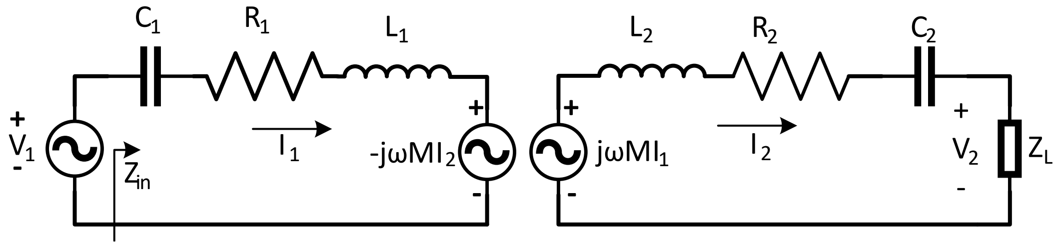

Figure 3.6 Equivalent circuit of an IPT system

where and $x_1 = \omega L_1$ - $\frac{1}{j\omega C_1}$ and $x_2 = \omega L_2$ - $\frac{1}{j\omega C_2}$ + x_L.

The analysis of the equivalent circuit helps definition of the voltage and current gains of the system. In addition to that, determination of the efficiency is obtained from the analysis of the equivalent circuit. The voltage gain of the system determines the secondary side voltage with respect to input voltage. The current gain determines the current value which is transferable to the secondary side. Hence, using equation (3.11) and (3.12), voltage equations on the primary side and secondary side can be written as;

$$V_1 = I_1 z_{in} = I_1 \left(z_1 - \frac{j\omega M I_2}{I_1} \right) \tag{3.13}$$

$$j\omega M I_1 = I_2 z_2 \tag{3.14}$$

In order to obtain the ratio between primary side current (I_1) and secondary side current (I_2) equation (3.14) gives the current gain (M) as shown in the following equation (Bojarski et al., 2014);

$$M_i = \left| \frac{I_2}{I_1} \right| = \left| \frac{j\omega M}{z_2} \right| \tag{3.15}$$

In the equation (3.13), the ratio between primary side current and secondary side current is equal to current gain. Hence, the equation for fundamental of primary side voltage can be rewritten as follows;

$$V_1 = I_1 \left(\frac{z_1 z_2 + \omega^2 M^2}{z_2} \right) \tag{3.16}$$

Therefore, it can easily be seen from equations (3.13) and (3.16), the input impedance equation across the primary side terminals is equal to (Liu et al., 2017);

$$z_{in} = \frac{z_1 z_2 + \omega^2 M^2}{z_2} \tag{3.17}$$

Using equation (3.14) and (3.16), the expressions of primary and secondary side currents are obtained as;

$$I_1 = \frac{z_2 V_1}{z_1 z_2 + \omega^2 M^2} \tag{3.18}$$

$$I_2 = \frac{j\omega M V_1}{z_1 z_2 + \omega^2 M^2} \tag{3.19}$$

The expression of the secondary side voltage V_2 can simply be written as;

$$V_2 = I_2 z_L \tag{3.20}$$

And the ratio between equations (3.16) and (3.20) determines voltage gain M_v (Mai et al., 2017);

$$M_v = \left|\frac{V_2}{V_1}\right| = \left|\frac{j\omega M z_L}{z_1 z_2 + \omega^2 M^2}\right| \tag{3.21}$$

If input impedance will be re-arranged;

$$z_{in} = z_1 + \frac{\omega^2 M^2}{z_2} = R_1 + jx_1 + \frac{\omega^2 M^2 (R_2 + R_L - jx_2)}{(R_L + R_2)^2 + x_2^2} \tag{3.22}$$

$$z_{in} = R_{in} + jx_{in} = R_1 + \frac{\omega^2 M^2 (R_2 + R_L)}{(R_L + R_2)^2 + x_2^2} + j\left(x_1 - \frac{\omega^2 M^2 x_2}{(R_L + R_2)^2 + x_2^2}\right) \tag{3.23}$$

It is obvious that input impedance is dependent on the loading condition. Furthermore, as it is seen from equations (3.15) and (3.21), the load affects voltage and current gains of the system. On condition that the primary side current is kept constant, secondary side current changes inversely proportional to the load impedance. For voltage gain, when load is changed, the variation of the numerator in equation (3.21) is bigger than the variation of the denominator (*i.e.* $\omega^2 M^2 \gg z_1 z_2$). Therefore, variation in voltage gain is in proportional to variation in the load.

The efficiency of the system is simply calculated as ratio between input and output powers. Here, the square of current gain is used as shown in the following equation while calculating efficiency. The efficiency formulation is shown as follows (Berger et al., 2015; Liu et al., 2017);

$$\eta = \frac{P_{out}}{P_{in}} = \frac{R_L}{R_{in}} \frac{|I_2|^2}{|I_1|^2} \tag{3.24}$$

$$\eta = \frac{\omega^2 M^2 R_L}{R_1 (R_2 + R_L)^2 + R_1 x_2^2 + \omega^2 M^2 (R_2 + R_L)} \tag{3.25}$$

As seen from equation (3.25), compensation on secondary side is vital for efficiency. If the system is made to run at primary side resonance frequency, system efficiency is decreased with respect to secondary side resonance condition. On the other hand, if the system is run at secondary side resonance frequency, the effect of x_2 on the efficiency is eliminated. As a result of that, efficiency is increased. The efficiency expression for this condition (*i.e.* $x_2 = 0$) is shown as follows (Kato et al., 2013; Bertoluzzo et al., 2015; Bojarski et al., 2014);

$$\eta = \frac{\omega^2 M^2 R_L}{R_1 (R_2 + R_L)^2 + \omega^2 M^2 (R_2 + R_L)} \tag{3.26}$$

Here, as mentioned before, while load is increasing, current gain decreases and voltage gain increases. Nevertheless, there is a maximum efficiency point at η - R_L graph. The load value at maximum efficiency point is called as optimum load value. Moreover, this value is calculated with first derivation of efficiency by R_L. If numerator and denominator is normalised with numerator, equation (3.26) becomes (Berger et al., 2015);

$$\eta = \frac{1}{1 + \frac{R_2}{R_1} + \frac{R_1 (R_2 + R_L)^2}{R_L (\omega M)^2}} \tag{3.27}$$

If the denominator is at the smallest value, then, efficiency is at maximum value. Hence;

$$\frac{\partial denum(\eta)}{\partial R_L} = \frac{\partial}{\partial R_L}\left(1 + \frac{R_2}{R_1} + \frac{R_1 (R_2 + R_L)^2}{R_L (\omega M)^2}\right) \tag{3.28}$$

Therefore;

$$\frac{\partial denum(\eta)}{\partial R_L} = \frac{R_1}{(\omega M)^2} - \frac{R_2^2 R_1}{(\omega M)^2 R_L^2} - \frac{R_2}{R_L^2} \tag{3.29}$$

$$R_{L.opt} = \sqrt{R_2^2 + \frac{R_2}{R_1}\omega^2 M^2} \tag{3.30}$$

In equation (3.27), if the assumption that R_L is much larger than R_2 is used, then R_2 is eliminated in equation. Thus, square of R_2 is omitted in equation. In addition to this, if coils are designed identically, then R_1 and R_2 will be equal to each other. Thus, the equation (3.30) turns into $R_{L,opt} \approx \omega M$ (Bojarski et al., 2014).

3.4.1 Analysis with Constant Frequency and Varying Load Resistance

The analysis of the system with respect to load variation under constant operating frequency is shown in Figure 3.7. The coil parameters are given in Table-3.1. The parameters are obtained from the study of Tezcan et al. (2017). Nevertheless, in this study, coils are designed for 150 *mm* distance and 0.2 coupling coefficient. Throughout experimental study, coils were set 75 *mm* distance and 0.45 coupling coefficient so as to decrease the magnetizing current (Gürbüz et al., 2017).

In Figure 3.7 (a), analysis is given for 0.2 coupling coefficient and in Figure 3.7 (b), analysis is given for 0.45 coupling coefficient. It can be observed that when coupling coefficient is decreased, maximum efficiency is decreasing whereas, transferred power increases. Furthermore, when coupling coefficient of the coils is decreased, mutual inductance in the coil system diminishes. This causes decrease at optimal load value as shown in equation (3.30). The optimal load value, as mentioned before, is the load value at the maximum efficiency point. Thus, maximum efficiency point diminishes. In addition to that, system efficiency is equal to multiplication of voltage and current gains, while there is not circulating reactive power in the system. Therefore, optimal load value and maximum efficiency points are seen at the point where voltage and current gains are close each other.

When dc load resistance is kept constant and conduction angle is changed, it has same affect with changing load value while conduction angle is equal to π. It is assumed that dc load is equal to R_{dc} and conduction angle is changed from 0 to π, according to equation (3.3), apparent load is changed from 0 to $(8/\pi^2)R_{dc}$. Furthermore, change of load characteristic has sinusoidal shape, as shown in Figure 3.4 and equation (3.3).

3.4.2 Analysis with Constant Load Resistance and Varying Frequency

Figure 3.8 is illustrating efficiency, voltage-current gains and input-output power with respect to variation of the operating frequency for k=0.2 and k=0.45 coupling

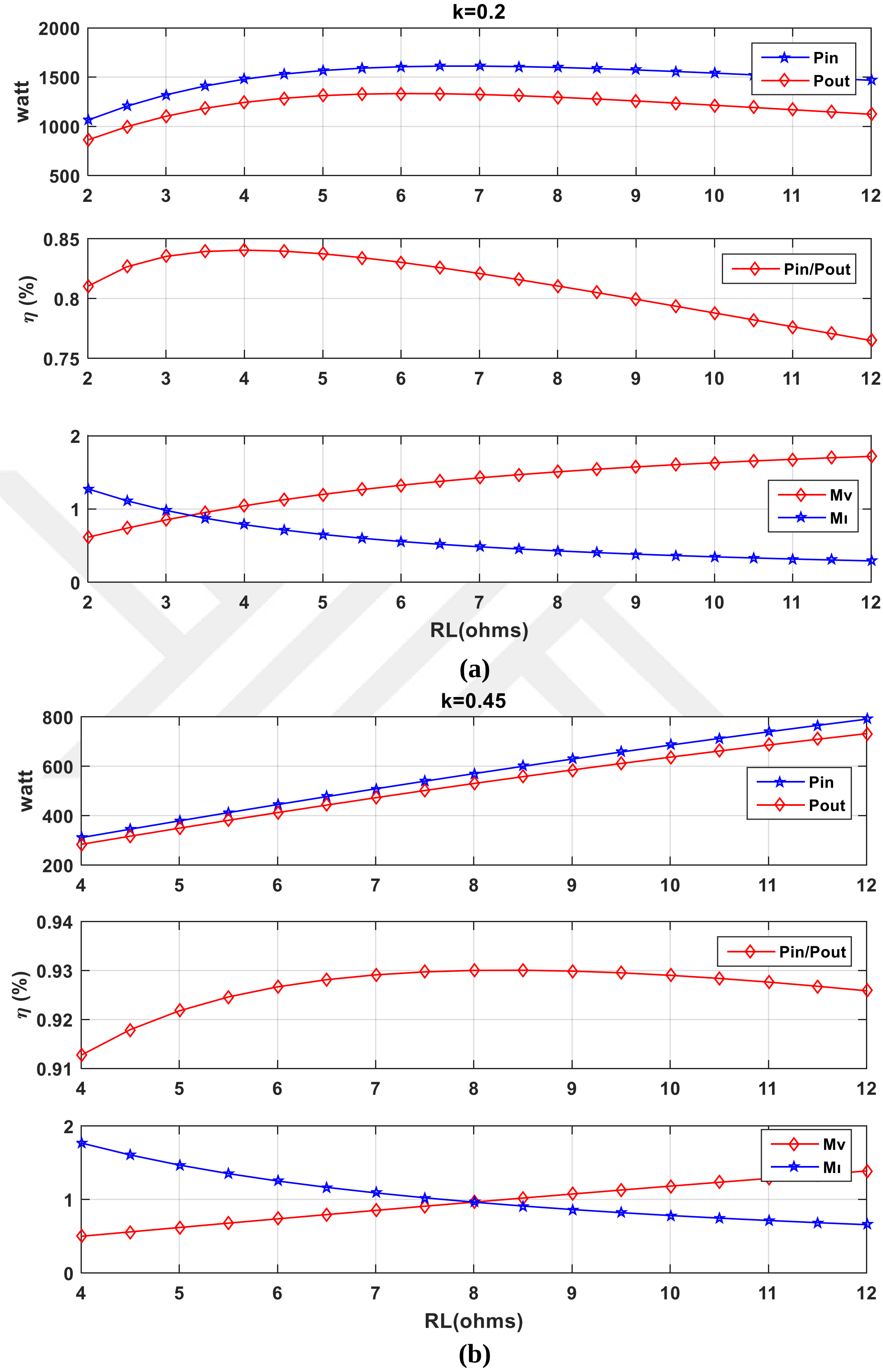

Figure 3.7 Analysis of the system with respect to variation of the R_L; input and output power, efficiency, voltage and current gains for a) k=0.2 b) k=0.45 (V_{in} = 75 V, f_o = 20.6 kHz, f_{res} = 19.62 kHz)

Table 3.1 Parameters of the system applied primary side control methods

Parameters	Description	Value
k	Coupling coefficient	0.45
C_1, C_2	Resonant capacitors	470 nF
L_1, L_2	Self inductance of coils	138 μ H
R_1, R_2	Parasitic resistance of coils	0.9 Ω
f_o	Operating frequency	20.6 kHz

coefficient values. Normalization at the frequency axis is made on resonance frequency. As it can be seen from Figure 3.8, efficiency is higher at the frequency that is slightly higher than resonance frequency. From equation (3.25), increment of frequency affects both numerator and denominator. However, increment in numerator becomes larger than denominator until it reaches maximum point. Hence, efficiency is larger than the value which is at resonance frequency. In addition to this, any increase at coupling coefficient value results in increase at bifurcation as seen in Figure 3.8.

3.4.3 Analysis with Constant Input and Output Voltages

The investigated IPT system is operated under constant battery and input voltage at steady state condition. Here, conduction angle (β) controls the charge current of battery and affects the fundamental value of the secondary side voltage (V_2). Assuming inverter and rectifier circuits are lossless, change of load with respect to input voltage (V_{in}), output voltage (V_{out}) and conduction angle is analysed using voltage gain equation given in (3.21). The voltage gain for both purely resistive and phase shift switching is calculated according to input voltage, output voltage and conduction angle which are illustrated in Figure 3.3 as follows;

$$V_{1,peak} = \frac{4}{\pi} V_{in} \sin(\omega t) \tag{3.31}$$

$$V_{2,peak} = \frac{4}{\pi} \sin\left(\frac{\beta}{2}\right) V_{out} \sin(\omega t) \tag{3.32}$$

And M_v is calculated from the ratio of the equations;

$$M_v = \frac{V_{2,peak}}{V_{1,peak}} = \frac{V_{out}}{V_{in}} \sin\left(\frac{\beta}{2}\right) \tag{3.33}$$

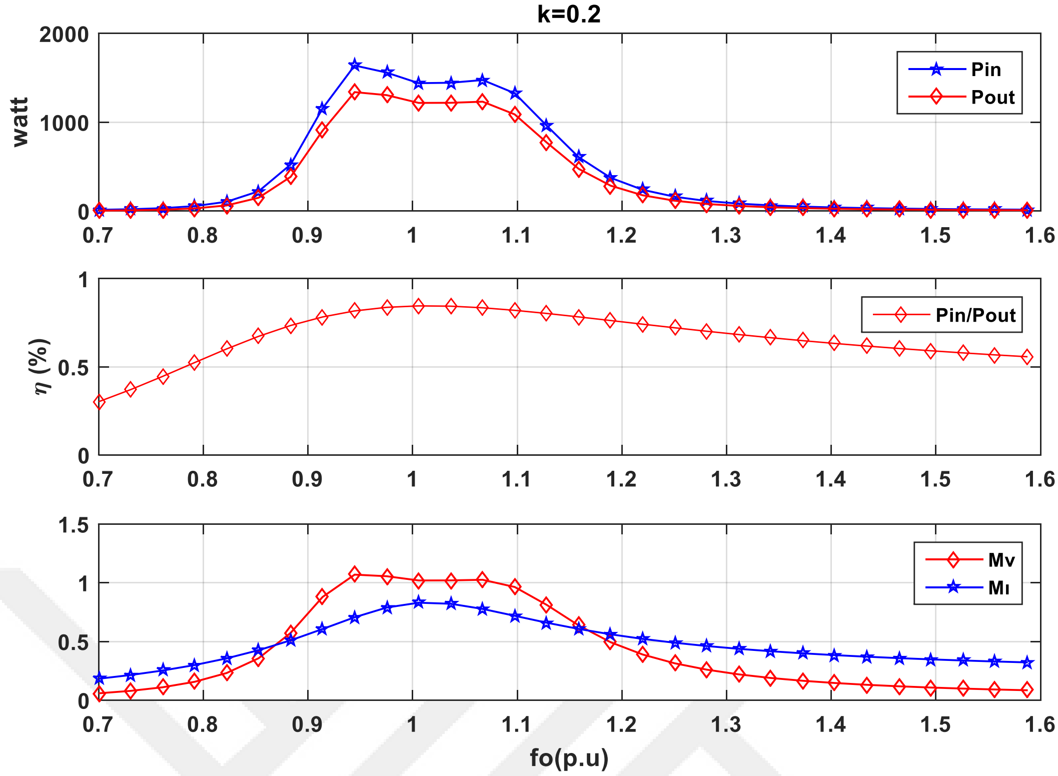

(a)

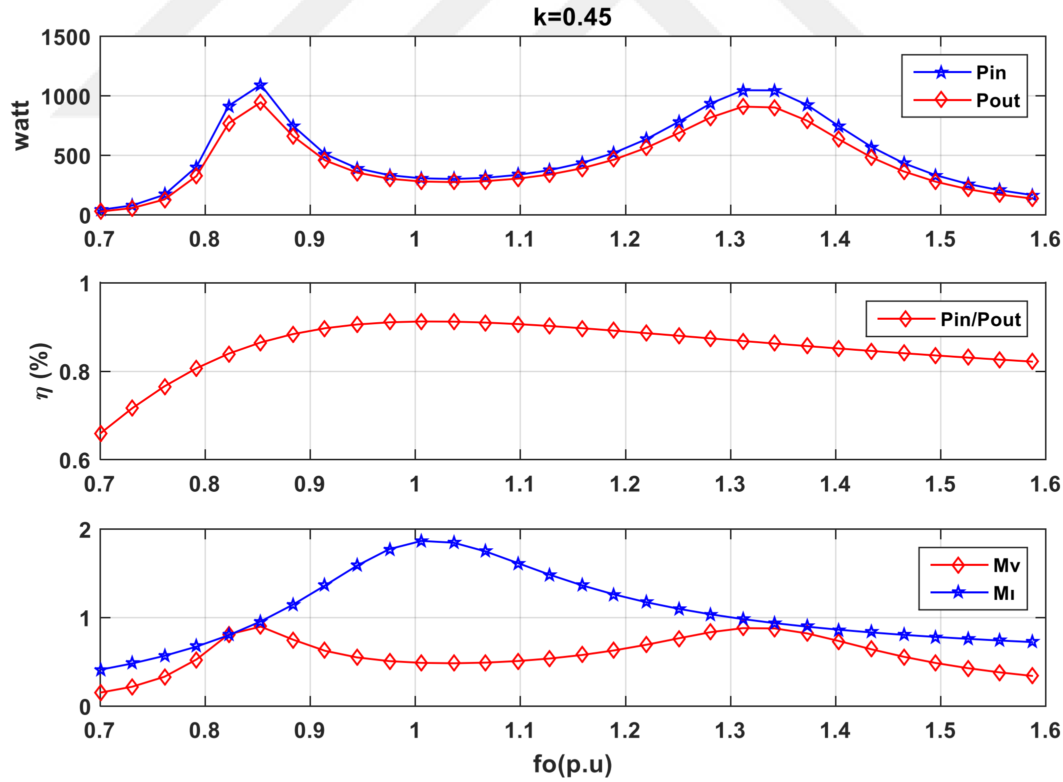

(b)

Figure 3.8 Analysis of the system with respect to variation of the operating frequency a) input and output power b) efficiency c) voltage and current gains (V_{in} = 75 V, k=0.45 R_{dc} = 4.8 Ω, f_{res} = 19.62 kHz)

As it can be seen from equation (3.33), conduction angle value affects voltage gain. On condition that the input impedance value seen from rectifier terminals is unknown, the load analysis of the system is calculated by rewriting equations (3.11) and (3.32) in (3.21) and edited as follows;

$$M_v = \left| \frac{j\omega M R_L}{j(X + x_1 R_L) + (R + R_L + R_1)} \right| \tag{3.34}$$

where $X = R_1 x_2 + x_1 R_2$ and $R = R_1 R_2 + \omega^2 M^2 - x_1 x_2$ and the load is purely resistive.

If equation (3.34) is squared and re-arranged, it becomes fourth degree equation of R_L. The equation and its coefficients are given as follows;

$$(a_4 - b_4)R_L^4 + (a_3 - b_3)R_L^3 + (a_2 - b_2)R_L^2 + (a_1 - b_1)R_L^1 + (a_0 - b_0)R_L^0 = 0 \tag{3.35}$$

Where coefficients are;

$a_4 = \omega^2 M^2\ (R_1^2 + x_1^2)$ $\quad$ $b_4 = M_v^2\ (R_1^4 + x_1^4 + 2R_1^2\ x_1^2)$

$a_3 = 2\omega^2 M^2\ (RR_1 + Xx_1)$ $\quad$ $b_4 = 4M_v^2\ (RR_1^3 + Xx_1^3 + RR_1 x_1^2 + Xx_1 R_1^2)$

$a_2 = \omega^2 M^2\ (R^2 + X^2)$ $\quad$ $b_2 = M_v^2\ (6R^2 R_1^2 + 6X^2 x_1^2 + 2(R^2 x_1^2 + 4RXR_1 x_1 + R_1 x^2))$

$a_1 = 0$ $\quad$ $b_1 = 4M_v^2\ (R^3 R_1 + X^3 x_1 + R^2 X x_1 + RR_1 X^2)$

$a_0 = 0$ $\quad$ $b_0 = M_v^2 (R^4 + X^4 + 2R^2 X^2)$

In this equation system, it is possible to have complex or negative roots. Nevertheless, only positive solutions are feasible for the system and just one positive solution is available.

When the load has reactive part, then, R_1, x_1 and M are replaced with R_1', x_1' and M' and expressions of the coefficients are given as follows;

$$R_1' = R_1(1 - \tan(\theta_1)\tan(\theta)) \tag{3.36}$$

$$x_1' = x_1 \left(1 + \frac{\tan(\theta_1)}{\tan(\theta)}\right) \tag{3.37}$$

$$M' = M\sqrt{1 + (\tan(\theta))^2} \tag{3.38}$$

where $\tan(\theta) = x_L/R_L$ and $\tan(\theta_1) = x_1/R_1$.

The load resistance is obtained using equation (3.35) for purely resistive control and for phase shift control, impedance expression is used. Figure 3.9 clearly shows that

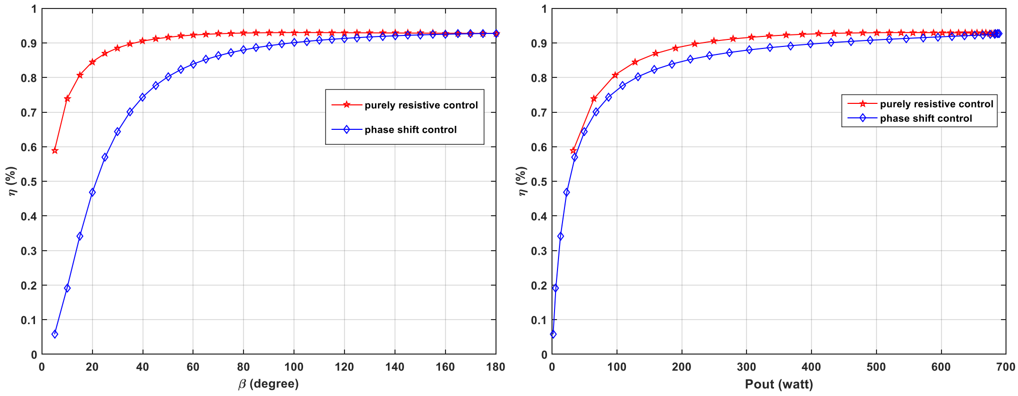

Figure 3.9 Coil efficiency and output power comparison for phase shift and purely resistive control (f_o = 20.6 kHZ V_o = 96 V)

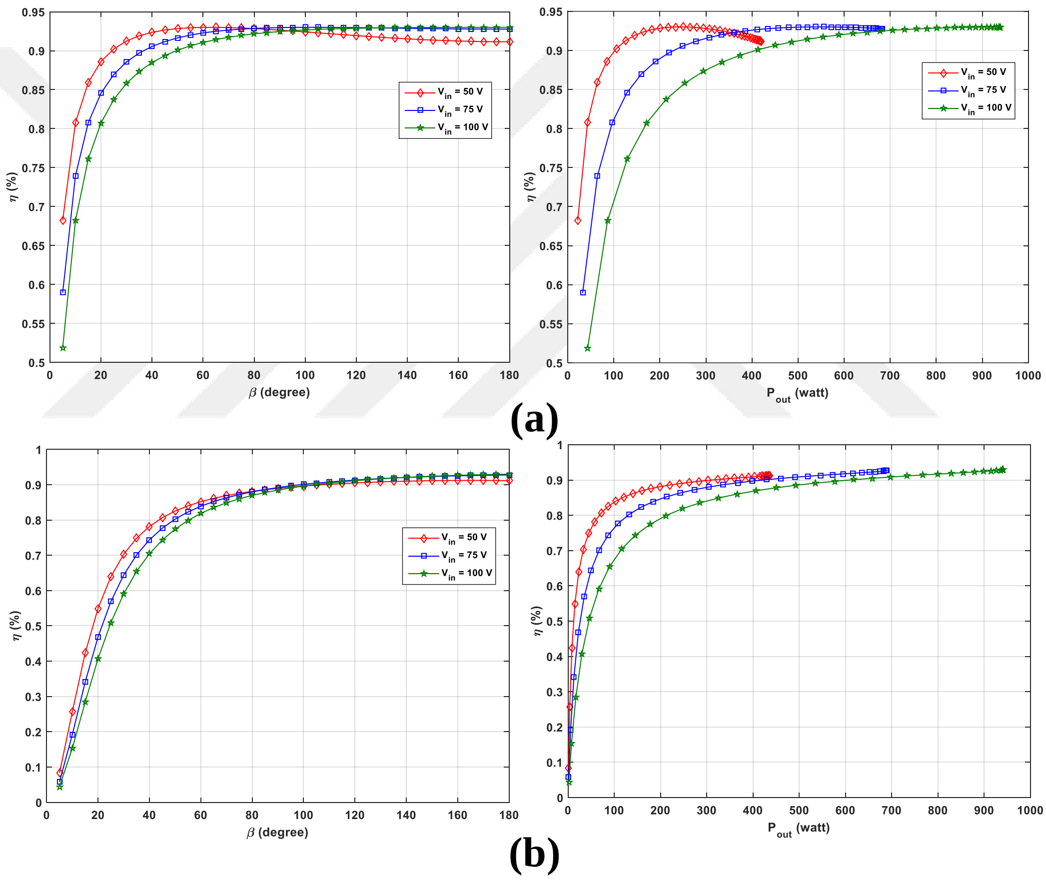

Figure 3.10 Variation of coil efficiency with respect to β and output power under constant battery voltage and different voltage gain conditions (f_o = 20.6 kHZ V_o = 96 V)

purely resistive control provides larger working range for high efficiency according to phase shift control.

It can be observed from Figure 3.10 that efficiency values at the first angle are different from each other. While the analysis which has 50 V input voltage catches maximum efficiency point at lower angle value, the analysis which has 75 V input voltage catches maximum efficiency point higher angle value. However, 100 V analysis does not have maximum efficiency point. In this analysis, fundamental value of secondary side voltage is kept constant at the lowest angle value for all input voltage values. When input voltage is changed, it causes a variation on both effective resistance value of battery and voltage gain. This results in same impact with given analysis in Section 3.4.2 and shown in Figure 3.7. Thus, it can be said that operation at 50V is the closest one to optimal load value and operation at 100V is beyond the maximum efficiency point.

3.5 Analysis of Other Control Methods

3.5.1 Analysis with Constant Input-Output Voltage by Primary Side Control Only

As mentioned before, alpha (α) control is a control type which is applied on primary side by changing conduction angle of inverter circuit. In this section, primary side α control impact on coils is analysed.

Control analysis is based on keeping charge current constant. Starting from output toward input, first, secondary side current peak value is calculated according to output current as follows;

$$I_{2,peak} = I_{out}\frac{\pi}{2} \tag{3.39}$$

For coil analysis, assuming that converters are lossless, output power is equal to secondary side power. Using this idea, secondary side voltage peak is calculated as;

$$V_{2,peak} = \frac{P_2}{I_{2,peak}} \tag{3.40}$$

After that, using analysis in Section 3.4, primary side voltage and current is calculated. Finally, input voltage is calculated according to conduction angle using;

$$V_{in} = \frac{\pi}{4\sin\left(\frac{\alpha}{2}\right)}V_{1,peak} \tag{3.41}$$

On condition that input voltage calculated using equation (3.41) is different from predefined one, α value is changed and iteration is applied.

Figure 3.11 is illustrates efficiency-alpha angle relation for this control method. Each point shows a current value. Because of the sinusoidal wave form, each point diverges from each other while power value is increasing. Figure 3.12 illustrates efficiency-output power.

3.5.2 Analysis with Constant Input-Output Voltage by Dual Side Control Analysis

In this section, effect of dual side control is investigated on coil efficiency. This control method is combination of α control and β control. Secondary side circuit applies a β conduction angle. In the analysis, likewise primary side α control, first step of process is to calculate secondary side current using following equation;

$$I_{2,peak} = \frac{\frac{\pi}{2} I_{out}}{\sin\left(\frac{\beta}{2}\right)} \tag{3.42}$$

After that, the other steps given in Section 3.4 are applied in calculation until $V_{1,peak}$ is calculated. In order to calculate primary side control angle, equation (2.6) is used. Using primary side voltage peak value and angle α, input voltage value is calculated on equation (3.41). If calculated input voltage does not equal to desired input voltage, iteration is applied on β.

Figure 3.13 illustrates relation between α and β on output power. From equation (2.6), it is obvious that relation between α and β angles is dependent on input and output voltage. Because of the voltage gain is less than 1, primary side control angle must be larger than secondary side control angle. Furthermore, at partial loads, coil efficiency does not decrease in contrast to primary side and secondary side controls.

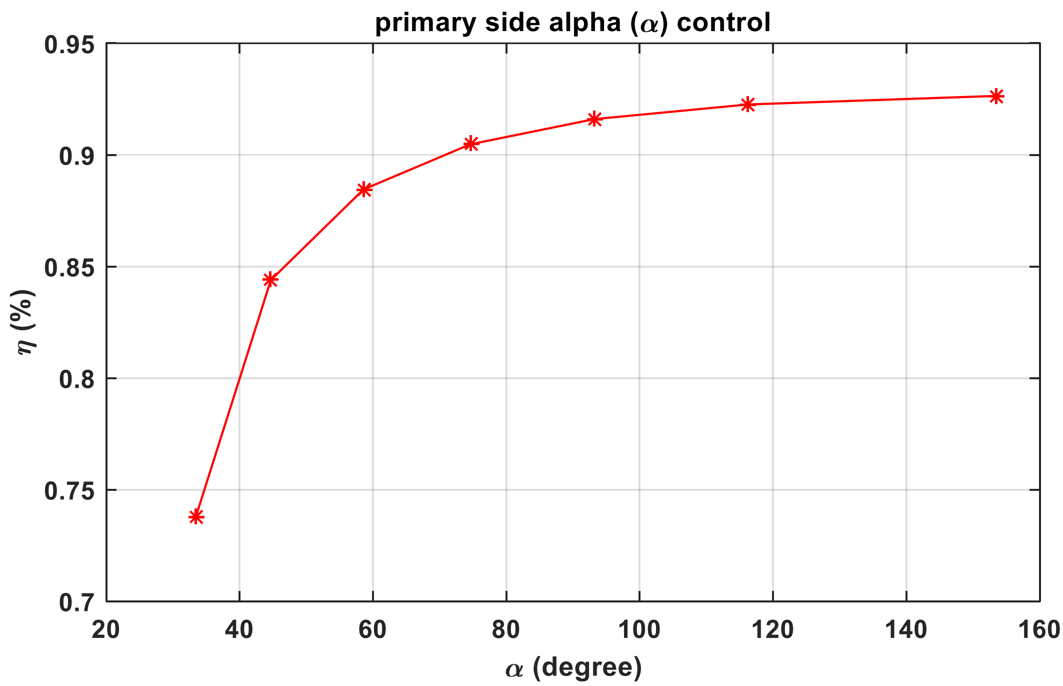

Figure 3.11 Primary side control efficiency-alpha graph (V_{in} =75 V, V_{out} = 96 V)

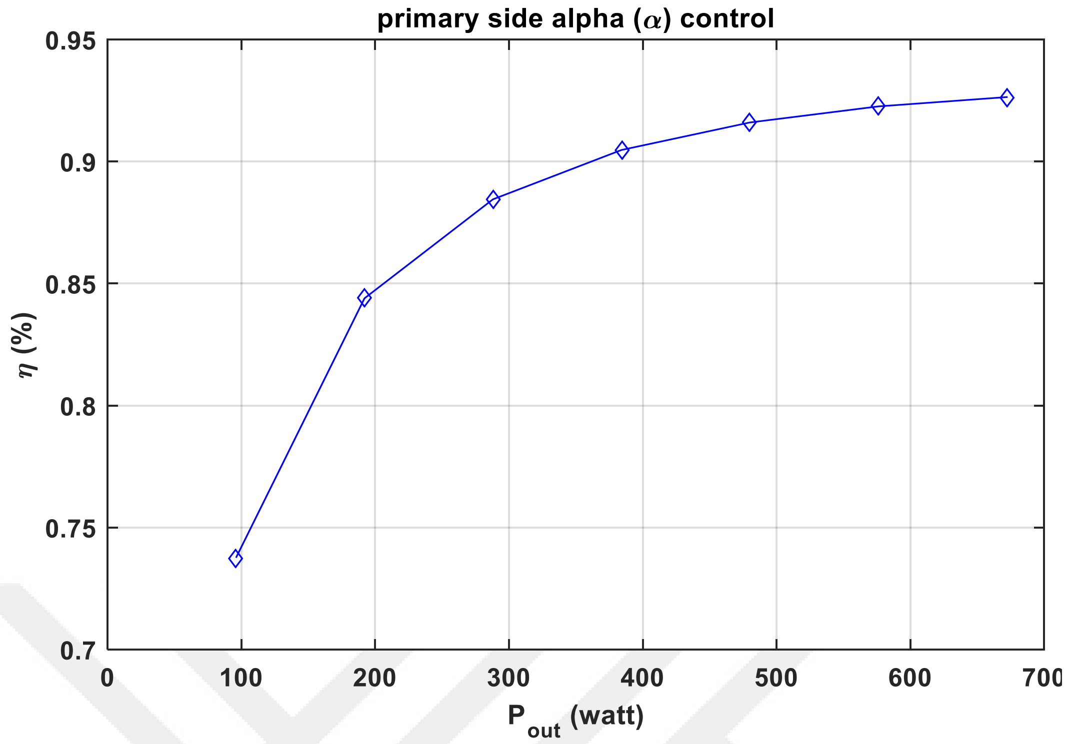

Figure 3.12 Primary side control efficiency-output power graph (V_{in} =75 V, V_{out} = 96 V)

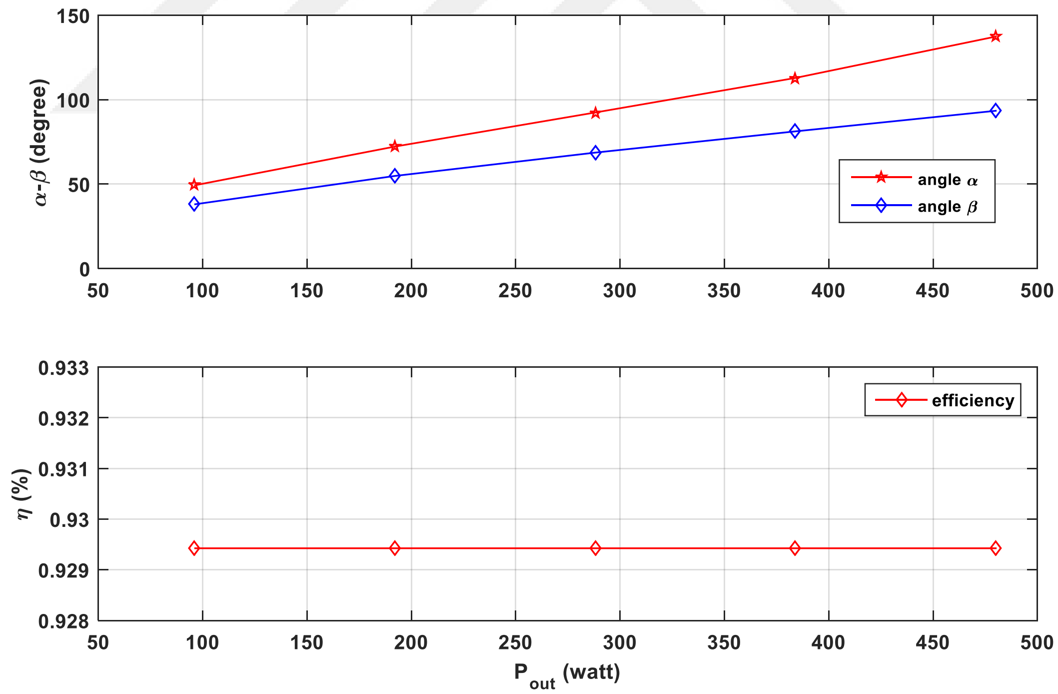

Figure 3.13 Dual side control method angle comparison and efficiency analysis (V_{in} =75 V, V_{out} = 96 V)

3.5.3 Efficiency Comparison of Control Methods

General logic of primary side control method is to supply desired power to the system by keeping current in desired range. For secondary side control method, it is to keep constant the charge current by changing apparent impedance seen from input terminals of the rectifier circuit. However, the common ground for both control methods is to supply constant charge current to the load. In contrast to primary side control method, secondary side control limits the charge current on secondary side. Dual side control tries to warranty that the system runs at its nominal condition. On that condition, both α and β values are vital for the system, besides ratio of input and output voltages. The ratio between input and output voltage defines voltage gain of the system. Thus, voltage gain is vital parameter for efficiency.

In general aspect about secondary side control is that secondary side control is suitable for the systems which have multi-pick up circuit (Kazmierkowski & Moradewicz, 2012; Li & Mi, 2015). However, as seen in Figure 3.14 (a), secondary side control can be more effective in terms of efficiency. When system voltage gain is bigger than 1, current gain becomes lower. On that condition, losses on secondary side coil becomes lower and this causes increment of efficiency.

In Figure 3.14 (b), voltage gain is equal to 1. For secondary side control, when conduction angle is low, secondary side current is high. Thus, losses are higher than primary side. On the other hand, when conduction angle close to π, secondary side current gets lower and so are losses. Because of that, efficiency of secondary side control method gets closer to primary side efficiency in Figure 3.14. When voltage gain is made smaller than 1, current gain becomes bigger than 1. That makes losses increased and this condition can be observed from Figure 3.14 (c).

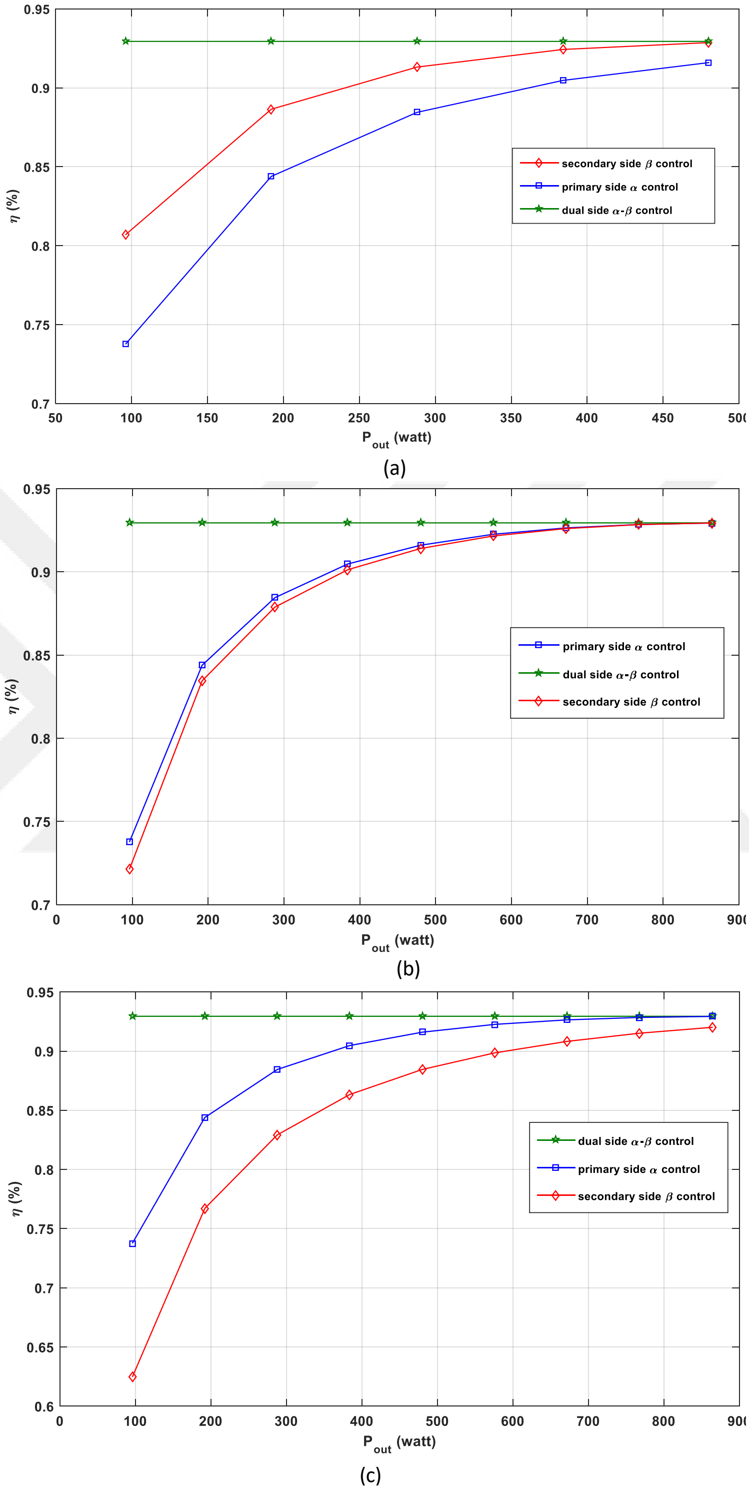

Figure 3.14 Coil efficiency for dual side, primary side and secondary side control methods for a) V_{in} =75 V, V_{out} = 96 V b) V_{in} =96 V, V_{out} = 96 V c) V_{in} =120 V, V_{out} = 96 V

CHAPTER FOUR
ANALYSIS OF THE SWITCHING AND CONDUCTION LOSSES

There are two major loss types in the IPT system. One of them is converter switching and conduction losses and the second one is resonant circuit losses (including coil and capacitor resistances). In chapter three, efficiency calculations are made assuming that the inverter and rectifier circuits are lossless. In this chapter, converter losses are considered in the analysis to evaluate system performance in more detail. In order to account for the losses of diodes and IGBTs, their characteristic are modelled as piecewise linear so as to simplify analysis. The details of converter loss analysis are given in the following subsection.

4.1 Linearization of the Diode and IGBT Characteristics

The typical diode and IGBT voltage drop model consists of a threshold voltage value and the variable voltage value obtained by multiplication of dynamic resistor value and current value passed through semi-conductor as shown below (Farzaneh & Nazarzadeh, 2009);

$$V_f = V_{fo} + R_f I_f \tag{4.1}$$

$$V_{ce} = V_{ceo} + R_{ce} I_c \tag{4.2}$$

where V_{ce} is voltage drop on IGBT, V_{ceo} is threshold voltage, R_{ce} is dynamic resistor value and I_c is collector current for IGBT V_f is voltage drop on diode, V_{fo} is threshold voltage, R_f is dynamic resistor value and If is collector current for diode. Figure 4.1 illustrates linearization of IGBT and diode characteristics. In order to linearize characteristics of semi-conductors, current interval that is worked in must be determined. According to pre-determined current limits, voltage values in response to current limits are found from V_f-I_f and V_{ce}-I_c graphs. And then, dynamic resistor value for diode (R_f) and IGBT (R_{ce}) are (Kolar et al., 1995);

$$R_f = \frac{\Delta V_f}{\Delta I_f} = \frac{V_{f2} - V_{f1}}{I_{f2} - I_{f1}} \tag{4.3}$$

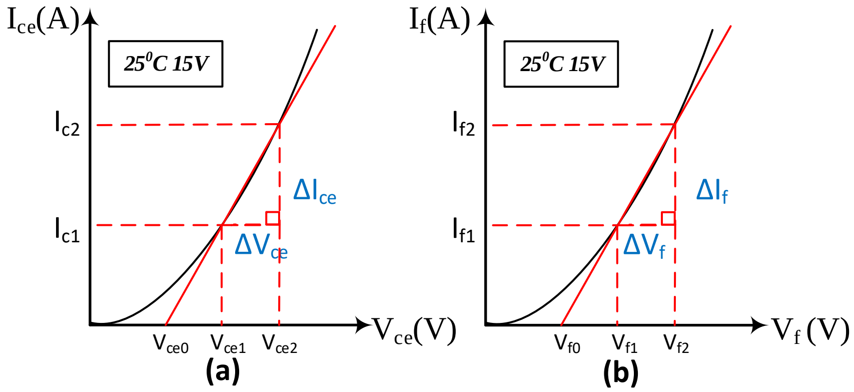

Figure 4.1 Linearization of semiconductors' voltage-current characteristic a) IGBT b) diode

$$R_f = \frac{\Delta V_{ce}}{\Delta I_c} = \frac{V_{ce2} - V_{ce1}}{I_{c2} - I_{c1}} \tag{4.4}$$

and for threshold voltage for diode (V_{fo}) and IGBT (V_{ceo}) (Kolar et al., 1995);

$$V_{fo} = \frac{V_{f1} I_{f2} - V_{f2} I_{f1}}{I_{f2} - I_{f1}} \tag{4.5}$$

$$V_{ceo} = \frac{V_{ce1} I_{c2} - V_{ce2} I_{c1}}{I_{f2} - I_{f1}} \tag{4.6}$$

Parameter values given in Table 4.1 are calculated according to determined characteristics in datasheet of IGBT and body diode used in inverter and rectifier.

Table 4.1 FGH15T120SMD IGBT and body diode model parameters

Parameters	Description	Value
V_{ce}	Forward IGBT voltage	1.05 V
R_{ce}	IGBT on state resistance	0.0417 Ω
V_{fo}	Forward diode voltage	1.9 V
R_f	Diode on state resistance	0.06 Ω

The curves given in Figure 4.1 are at a specific temperature. In this study, 25^0C curve is used because of the low operating temperature value.

4.2 Switching and Conduction Loss Calculation

General view of the system of which losses are analysed is shown in Figure 3.1. In order to calculate switching and conduction losses, the idealized current and voltage waveforms are shown in Figure 4.2 for the inverter. Here, θ is the phase difference between the fundamental waveforms of primary voltage and current. The losses in inverter circuit depend on phase angle θ.

In order to calculate the conduction power loss on diodes, the voltage and current product is averaged over one cycle as follows;

$$P_{cond,D} = \frac{1}{T}\int_0^T V_f I_f(t) d(t) = \frac{1}{T}\int_0^T \left(V_{fo} I_f(t) + R_f I_f(t)^2\right) d(t) \tag{4.7}$$

where T is switching period of inverter and calculation of equation (4.7) is simplified as follows;

$$P_{cond,D} = V_{fo} I_{f,avg} + R_f I_{f,rms}^2 \tag{4.8}$$

This formulation can be used for IGBT conduction loss calculations as;

$$P_{cond,D} = V_{ceo} I_{c,avg} + R_{ce} I_{c,rms}^2 \tag{4.9}$$

The system operation frequency is slightly higher than natural frequency. Hence, there exist a phase difference between the fundamental primary voltage and current waveforms. Because of the phase shift, when an IGBT pair are switched on, current is opposite pole with voltage polarity throughout phase angle θ and it passes through their body diodes, as shown in Figure 4.2. On that condition, when switches are turned on, the current passes through switches is zero. Therefore, there are not turn-on switching

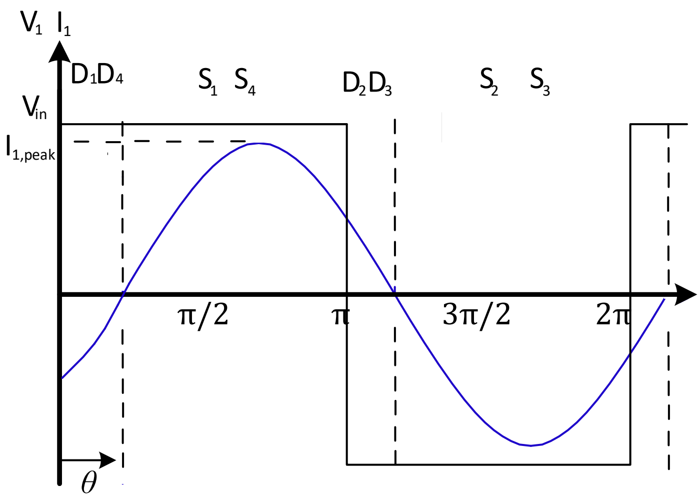

Figure 4.2 Voltage and current waveforms of inverter circuit

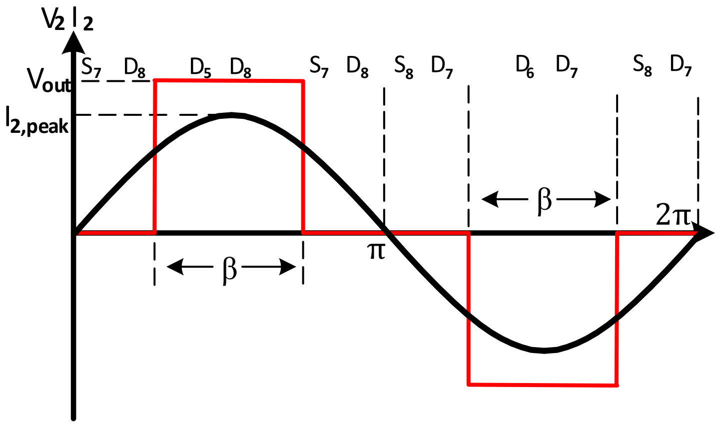

Figure 4.3 Voltage and current waveforms of rectifier circuit

losses in the inverter. For inverter circuit, waveforms are same for each IGBT and diode. Average value of diode current is;

$$I_{D,avg} = \frac{I_{1,peak}}{2\pi}\left[1-\cos(\theta)\right] \tag{4.10}$$

$$I_{D,rms} = \sqrt{\frac{I_{1,peak}^2}{2\pi}\left[\frac{\theta}{2}-\frac{\sin(2\theta)}{4}\right]} \tag{4.11}$$

$$I_{s,avg} = \frac{I_{1,peak}}{2\pi}\left[1+\cos(\theta)\right] \tag{4.12}$$

$$I_{s,rms} = \sqrt{\frac{I_{1,peak}^2}{2\pi}\left[\frac{\pi-\theta}{2}+\frac{\sin(2\theta)}{4}\right]} \tag{4.13}$$

Figure 4.3 illustrates secondary side active rectifier idealized input current and voltage waveforms. D_7 and D_8 diodes conduct throughout one half cycle, while D_5 and D_6 diodes conduct for β angle interval through each half cycle in sequence. S_7 and S_8 conduct at the angle value that is complement of β in same half cycle with D_5 and D_6 diodes in sequence.

Conduction and switching losses at secondary side inverter depend on conduction angle β. It does not only affect rectifier losses, but also affects coil and rectifier losses. Any increase in β causes a decrease in the peak magnitude of secondary current ($I_{2,peak}$). According to equivalent circuit, this results in increasing of $I_{1,peak}$ and conduction losses in inverter circuit. Because of this reason, losses in overall system highly depend on β.

In order to calculate losses in secondary side circuit, rms and average values of the switching devices currents are formulated as follows;

$$I_{D5,avg} = I_{D6,avg} = \frac{I_{2,peak}}{\pi}\sin\left(\frac{\beta}{2}\right) \tag{4.14}$$

$$I_{D5,rms} = I_{D6,rms} = \frac{I_{2,peak}}{2}\sqrt{\frac{\beta+\sin(\beta)}{\pi}} \tag{4.15}$$

$$I_{D7,avg} = I_{D8,avg} = \frac{I_{2,peak}}{\pi} \tag{4.16}$$

$$I_{D7,rms} = I_{D8,rms} = \frac{I_{2,peak}}{2} \tag{4.17}$$

$$I_{S7,avg} = I_{S8,avg} = \frac{I_{2,peak}}{\pi}\left[1-\sin\left(\frac{\beta}{2}\right)\right] \tag{4.18}$$

$$I_{S7,rms} = I_{S8,rms} = \sqrt{\frac{I_{2,peak}^2}{\pi}\left(\frac{\pi-\beta}{4}-\frac{\sin(\beta)}{4}\right)} \tag{4.19}$$

Due to resistive control, the switching strategy is based on hard switching. In other words, switched current and voltage are non-zero. Thus, there exist switching losses which are dependent on β. Switching losses are calculated with respect to datasheet values normalizing turn on and turn-off energy obtained in test condition. Wasted energy at switching moment is calculated as (Chen et al., 2016);

$$E_{SW,IGBT}(I) = (E_{on,IGBT} + E_{off,IGBT})(I_{nom}, V_{nom})\frac{I(t)V_{dc}}{I_{nom}V_{nom}} \tag{4.20}$$

According to equation (4.20), switching losses in rectifier circuit is obtained by multiplication of energy wasted at switching moment and switching frequency. Switching losses for the waveforms shown in Figure 4.3 is given as follows;

$$P_{SW7} = P_{SW8} = \frac{f\left(E_{on}+E_{off}\right)I_{2,peak}\sin\left(\frac{\pi+\beta}{2}\right)V_{out}}{I_{nom}V_{nom}} \tag{4.21}$$

where E_{on} and E_{off} are turn on and turn off energy losses of IGBT at switching instant for nominal test voltage V_{nom} and test current I_{nom} condition, respectively.

4.3 Experimental Verification of Semi-Conductor Losses

From Figure 4.4 to 4.6, switching wave forms are given for IGBTs and its body diodes. Upper side figures are IGBT voltage-current waveforms, lower side figures are the waveform of the diode which is connected upper side of the measured IGBT. Although it is intended to measure IGBT current, the current waveform of the next cycle is seen as negative half cycle instead of zero current; this condition can be observed in Figure 4.4, 4.5 and 4.6 at IGBT current waveforms. This negative half cycle is the current which passes through body diode of IGBT. Because IGBT current and body diode current are in opposite direction, while IGBT current is measured as positive half cycle, body diode current is measured as negative half cycle.

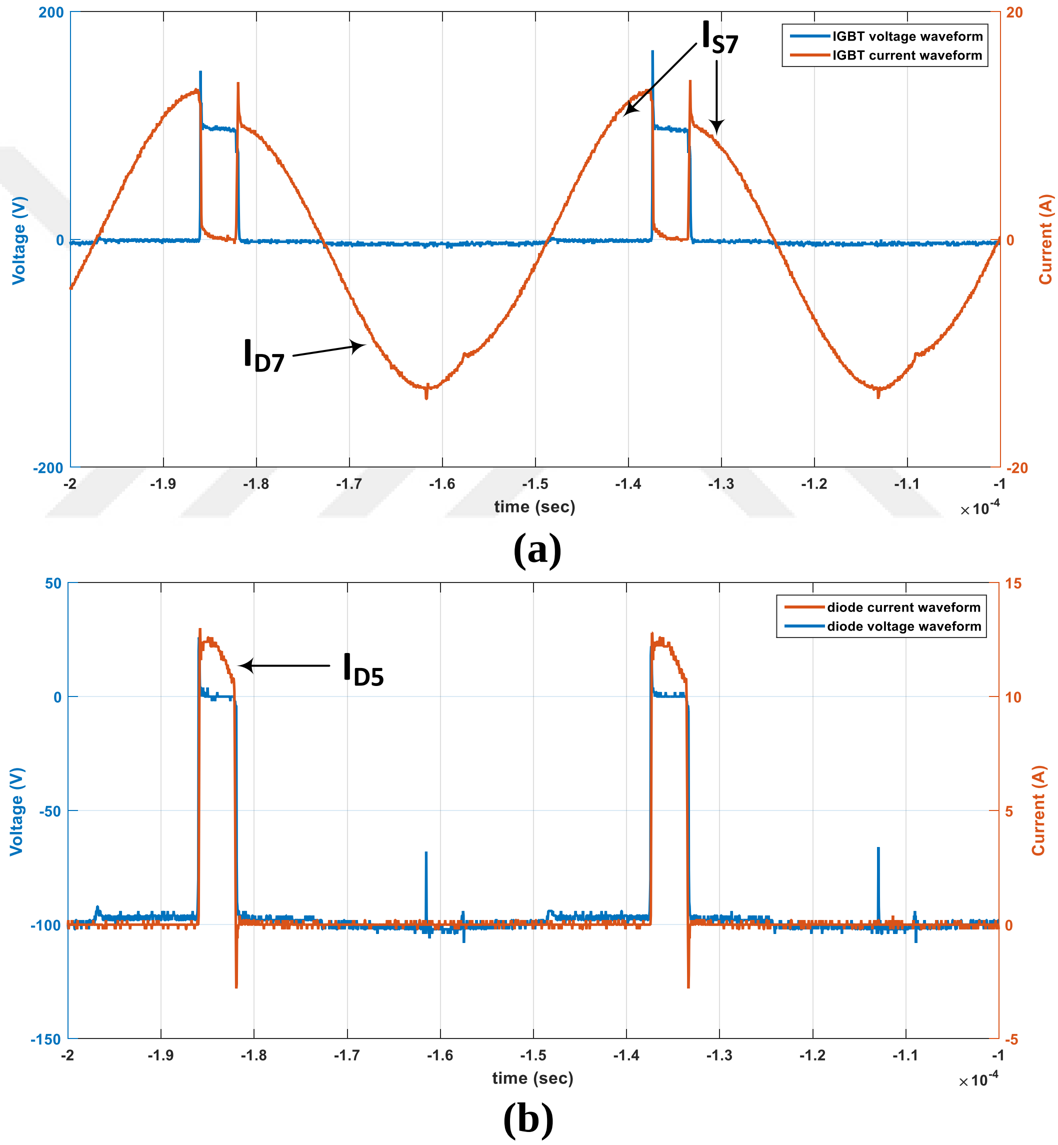

Figure 4.4 Switching voltage (blue ch2) and current (orange ch3) waveforms of switches at 30^0 with battery load a) waveforms of S7 switch and D7 body diode b) waveform for D5 diode

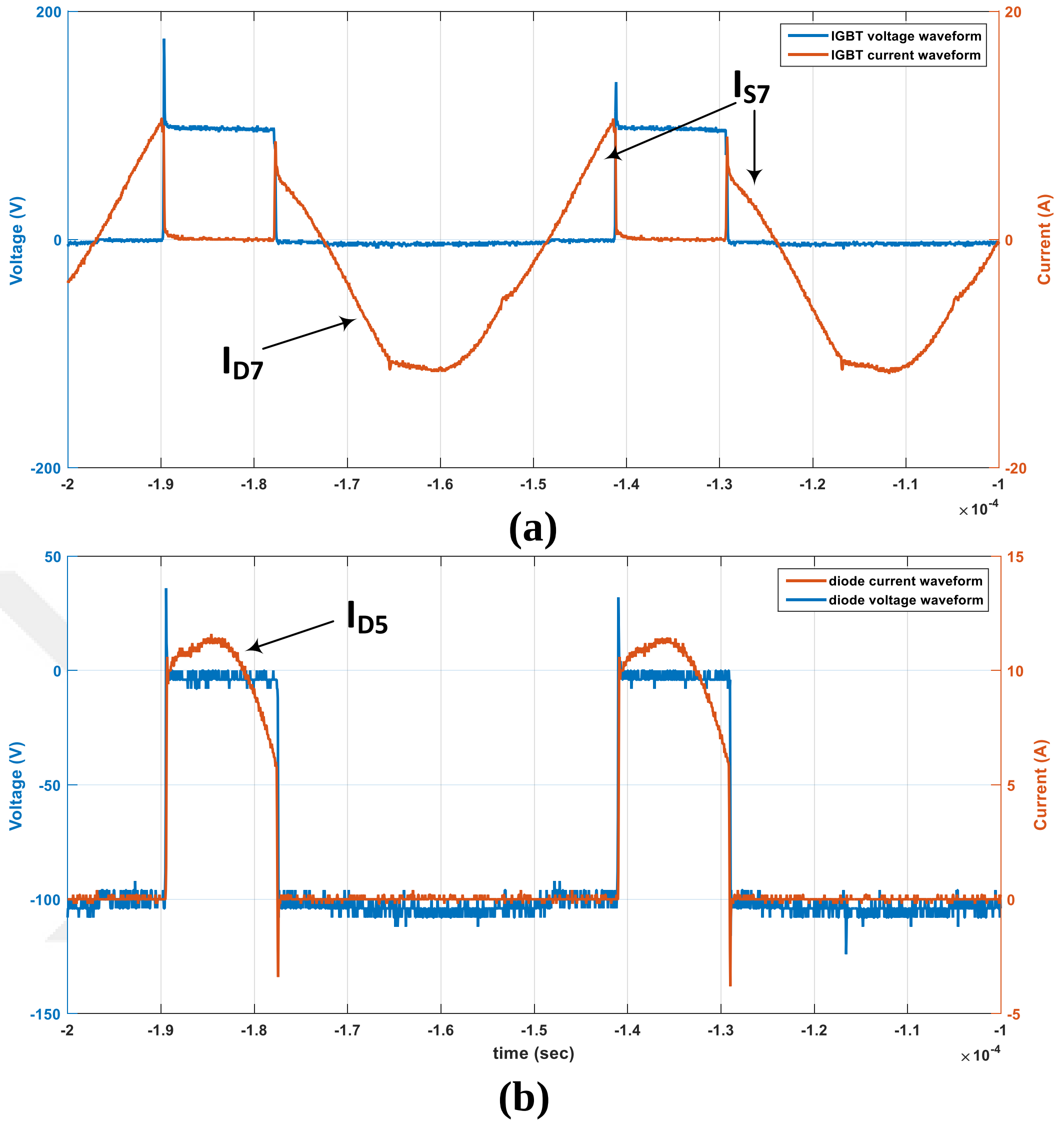

Figure 4.5 Switching voltage (blue ch2) and current (orange ch3) waveforms of switches at 90^0 with battery load a) waveforms of S7 switch and D7 body diode b) waveform for D5 diode

Comparison of switching and conduction losses is given in Figure 4.7 for one leg at resistive load. Diode and IGBT conduction losses are given together. Measurement results were gathered for 30^0 angle steps. It can be observed from Figure 4.7 that while conduction angle increases, conduction losses increase, since average current of diode increases and diode voltage drop is higher than IGBT voltage drop. Moreover, switched IGBT current peak value decreases while conduction angle is increasing. Hence, switching losses are in inverse proportion with conduction angle.

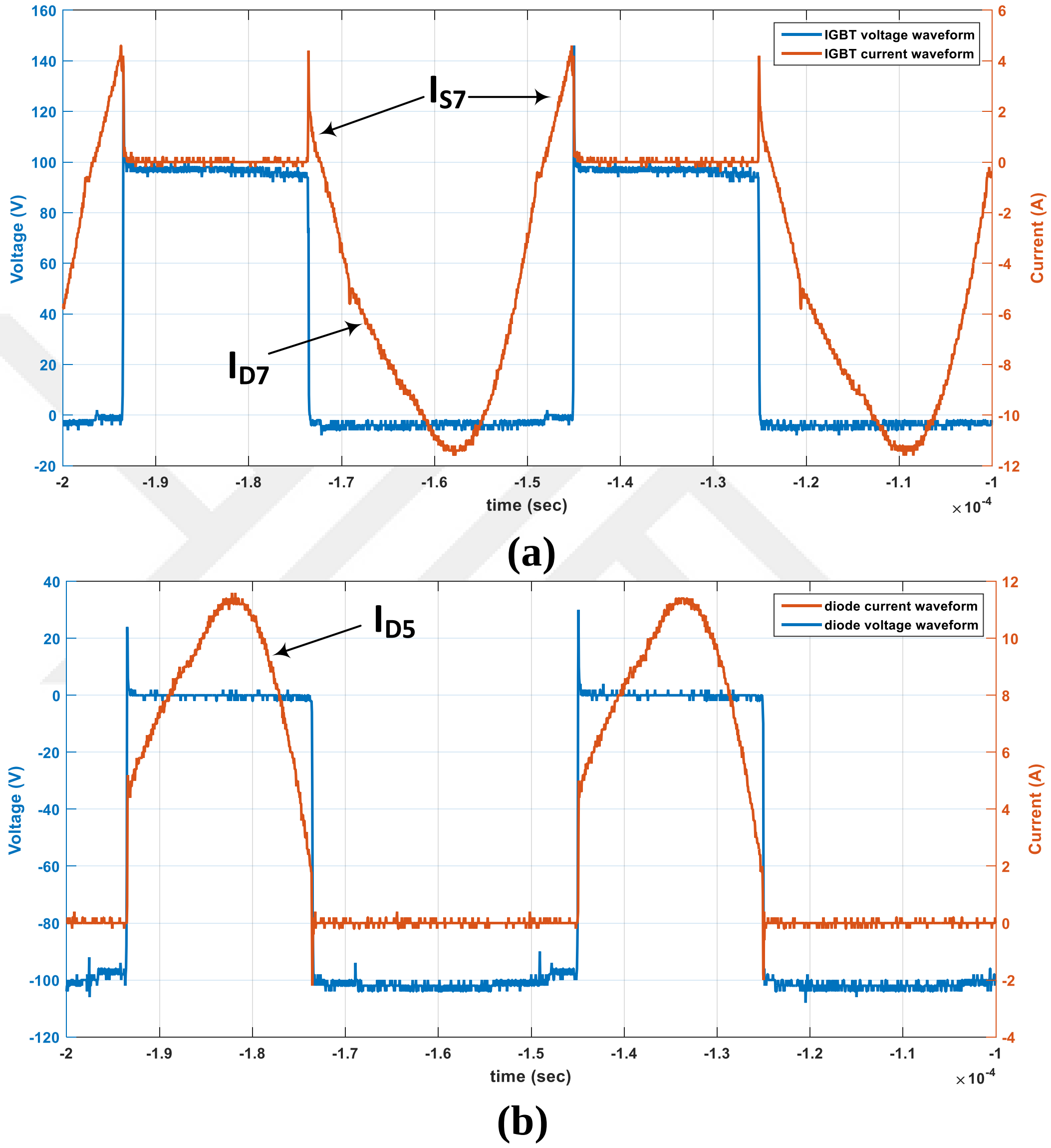

Figure 4.6 Switching voltage (blue ch2) and current (orange ch3) waveforms of switches at 150^0 with battery load a) waveforms of S7 switch and D7 body diode b) waveform for D5 diode

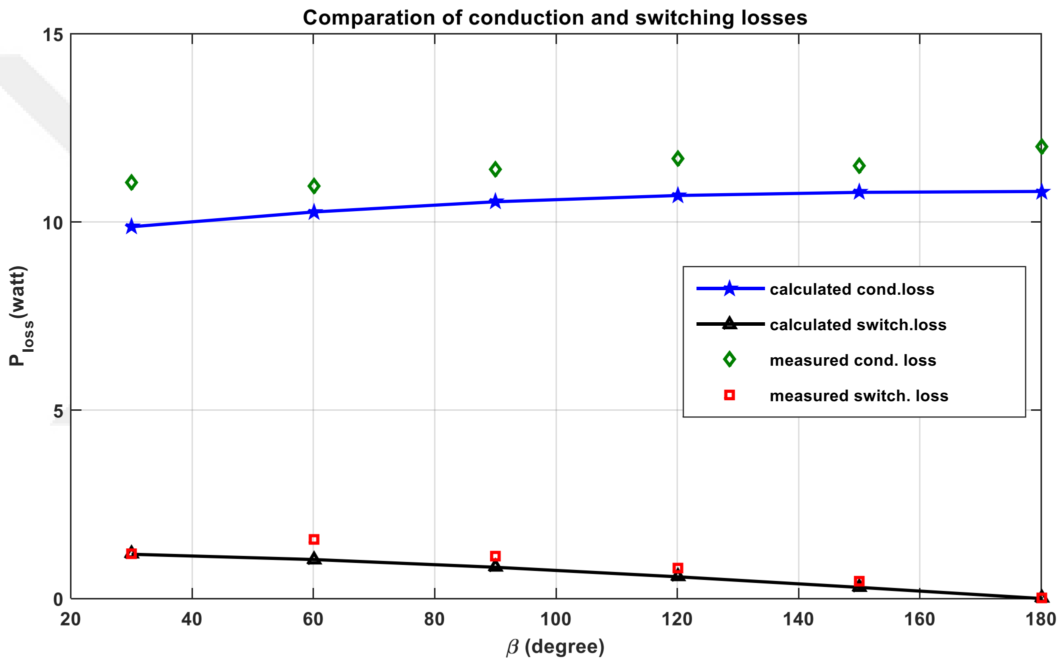

Figure 4.7 Comparison of conduction and switching losses for rectifier circuit (V_{in} = 50 V, R_{dc} = 16Ω)

CHAPTER FIVE
DESIGN AND IMPLEMENTATION OF SECONDARY-SIDE ACTIVE RECTIFIER

The proposed method and topology has been designed and implemented on a 2 kW IPT system prototype in laboratory conditions. The system of which block diagram is given in Figure 5.1 consists of a zero-crossing circuit, a voltage and current sensing circuit, power supply circuit for zero-crossing detector circuit and for the sensor circuit, gate driving circuit and main board which consists of the rectifier circuit. The circuits are controlled using Texas TMS320F28027 Launch PadTM microcontroller board. The rectifier circuit designed using FGH15T120SMD insulated gate bipolar transistor (IGBT). Each IGBT has anti-parallel diode as built in component. The rated values of IGBT are 1200V, 15A. In the following subsection, circuits of the system are explained.

Topology of main board which is designed as rectifier circuit is mentioned in Chapter III. In addition to the circuits before mentioned in previous paragraph, a place is reserved for the TMS320F28027 microcontroller card. Gate drive circuit is designed as it can easily be isolated from main board. The gating signals are given IGBTs by same opto-coupler from different channels. Control method and circuit diagrams for designed circuits are given in the following subsections. In addition, schematic and board drawings for the circuits are given in Appendix A.

5.1 Implementation of the Control Method

The control logic starts with detecting zero-crossing of secondary current on zero-crossing circuit. This zero-crossing signal is connected to the microcontroller's pin. Afterwards, zero-crossing signal generates an interrupt. In the interrupt service routine, the microcontroller detects the half period of secondary current and synchronizes the gating signals with the current. Figure 5.1 illustrates the block diagram of the process. After detecting half period of the secondary current value noted as T_S in Figure 5.1 and Figure 5.2, it is set as PWM counter period value.

In order to control battery charge current, a classic PI controller is used. When charge current I_{out} is sensed, error value is calculated according to reference value of charge current $I_{out-ref}$. PI controller generates conduction angle with respect to error as follows (Surgevil, 2004):

$$\beta(nT_{smp}) = \beta[(n-1)T_{smp}] + K_p[E(nT_{smp}) - E[(n-1)T_{smp}]] + K_i T_{smp} E(nT_{smp}) \quad (5.1)$$

where T_{smp} is sampling period, which is determined by timer-1 interrupt. In order to control the system in resistive mode, conduction angle is centred on secondary side current half period (T_S). In order to succeed that, values of the PWM comparator COMPA and COMPB are calculated as $(T_S - \beta)$ / 2 and $(T_S + \beta)$ / 2, respectively. When there is a match between PWM counter value and comparator value COMPA, action qualifier, that is a unit which restates the PWM signal according to coding, pulls the signal low level, while PWM counter is counting up. Likewise COMPA, when there is a match between COMPB and PWM counter value, action qualifier pulls the signal high level. By that way, conduction angle is centred on secondary side current half period so as to run the system in resistive mode.

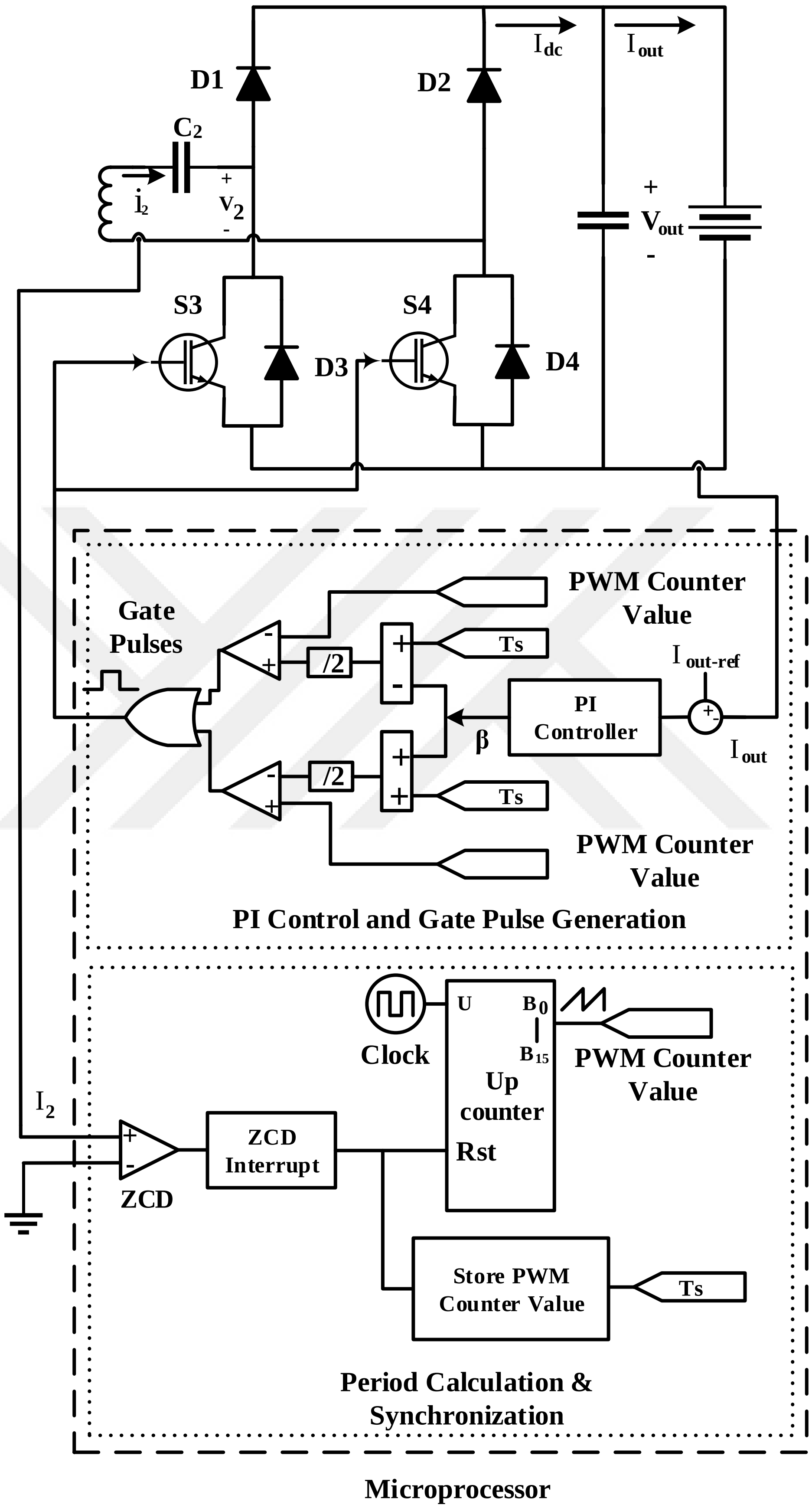

Figure 5.1 Control block diagram of the secondary side active rectifier

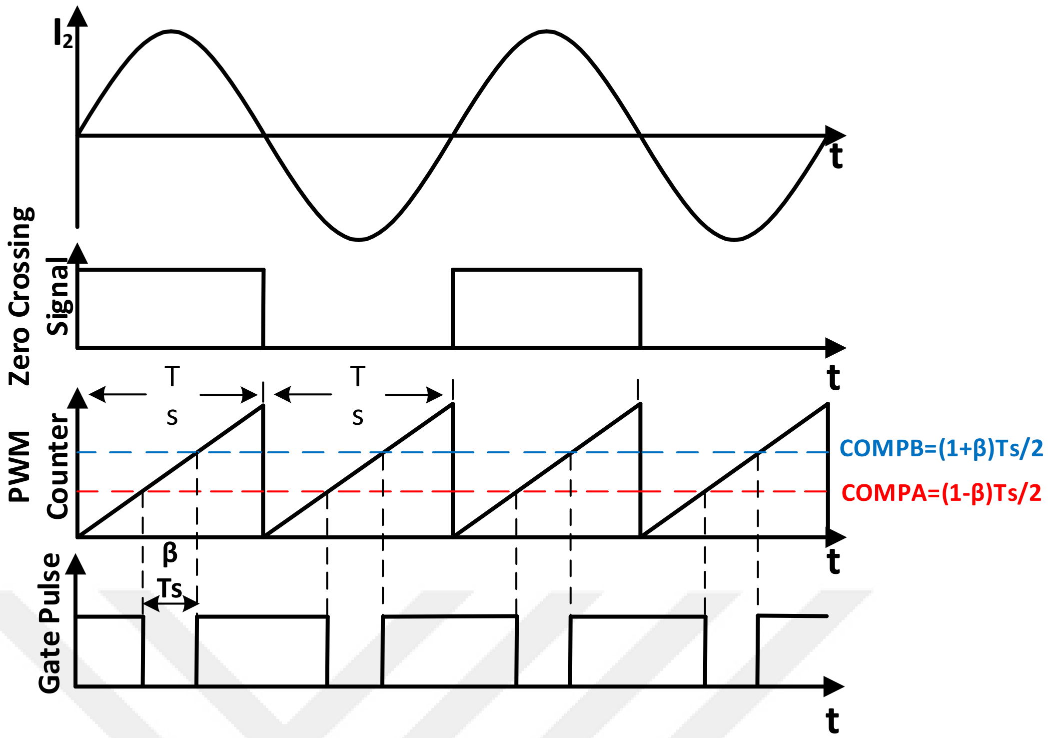

Figure 5.2 Waveform of the gate pulse generation process of the control circuit

5.2 Zero-Crossing Detector Circuit

The zero crossing detector circuit is designed so as to detect zero crossing of secondary current. In order to detect zero-crossing of secondary current, a current transformer is used because of the large bandwidth. In that way, phase delay between secondary current and detected current signal is blocked largely. Current transformer carries two different coils each of which has twenty turns. Obtained signal from current transformer is connected to the resistor named as R_1 in Figure 5.3 in order to

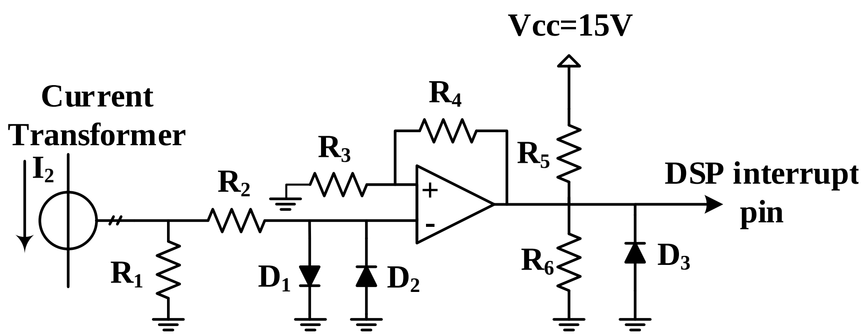

Figure 5.3 Zero-crossing detector circuit

generate output voltage. D_1 and D_2 diodes are used so as to limit the signal in a range. R_3 and R_4 resistors are used in order to add hysteresis band to zero-crossing signal to prevent incorrect signal because of the noise. Diode D_3 is connected to the output of the comparator circuit so as to eliminate high and low voltage values.

5.3 Voltage and Current Sensing Circuit

In order to obtain feedback signal for closed loop control, voltage and current sensing circuit is designed at dc bus. While designing sensor circuits, maximum output value of the circuit is set as 3.3 V due to analog to digital converter input range. Figure 5.4 and 5.5 show current and voltage sensing circuits, respectively. The offset and summing amplifier circuits are redesigned and added to both current and voltage sensing circuits in the study of Surgevil (2004). The current transducer LA-25 is designed so that it has 1/1000 gain value according to datasheet information. The current sensor generates an output current value from measurement pin M according to pin connection combination given in the datasheet. In order to generate output voltage, LA-25 needs a measurement resistor shown as R_m in Figure 5.4. According to current value generated at M pin and R_m value, sensor transforms the measured current into voltage data. Afterwards, current data is sent to buffer circuit.

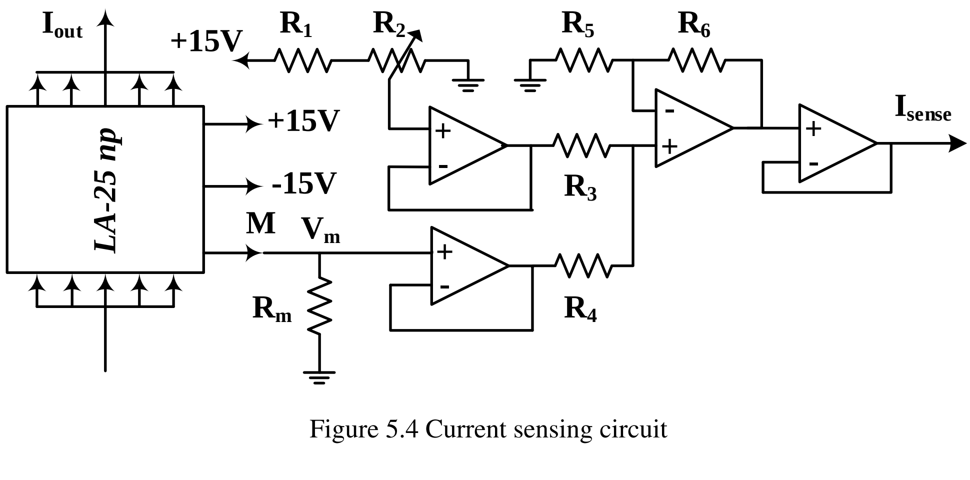

Figure 5.4 Current sensing circuit

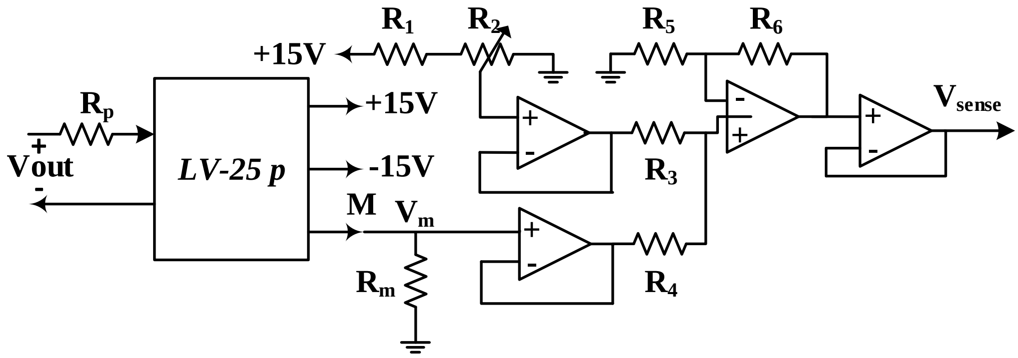

Figure 5.5 Voltage sensing circuit

The gain calculation of the sensor G_I is shown as follows;

$$G_I = \frac{1}{1000} R_m G_T \tag{5.2}$$

where G_T is the gain value of the summing circuit. The overall sensor gain is adjusted as $10mV/\text{A}$ using equation 5.2.

The voltage sensor LV-25 p needs a resistance on the primary side in order to sense the input voltage of the sensor. The voltage value of the sensor is determined by the primary side voltage, limitation resistance R_p and measurement resistance R_m. The gain calculation of the sensor G_v is shown as follows;

$$G_v = \frac{V_{out}}{R_P} \frac{2500}{1000} R_m \tag{5.3}$$

5.4 Gate Drive Circuit

Gate drive signals pass through an opto-coupler circuit. The gating signals of IGBTs are generated by microcontroller. After a resistor, the signals are sent to opto-coupler circuit using HCPL 2231 which has two channels in order to amplify the signal power. The resistor placed between microcontroller and opto-coupler is used so as to limit input current of opto-coupler.

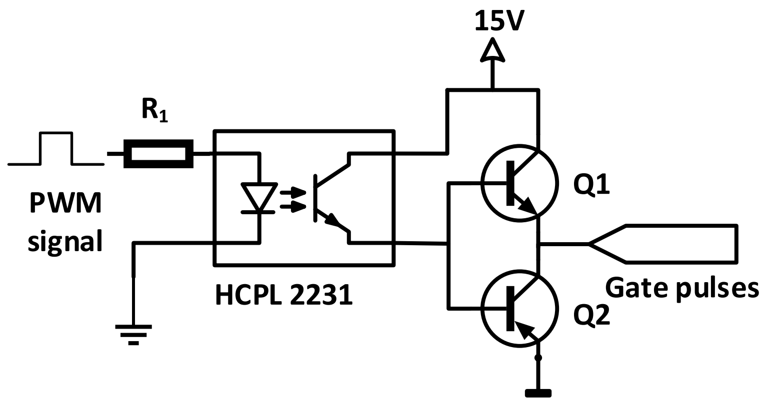

Figure 5.6 Opto-coupler circuit for one PWM channel

5.5 Software Design

In software programming, there are two interrupt which are tripzone interrupt (tzint) and timer-1 interrupt. The flow chart of the system is show in Figure 5.8.

Duty of tripzone interrupt is to synchronize gating signals and determine half period of secondary current. While program is running in main loop, the zero-crossing signal of secondary current is detected by zero-crossing detector circuit, this signal is sent to analog comparator which is available on microcontroller. According to output of the analog comparator, a digital comparator generates an event signal pre-defined as name and logic level. When this pre-defined event signal is generated by digital comparator, this signal causes an interrupt named tripzone.

When tripzone interrupt is generated, first, PWM comparator values are refreshed immediately, in case of conduction angle is quite close to π. On the condition that conduction angle is quite close to π and PWM comparator values are refreshed after a few line of code, PWM counter may exceed the refreshed CMPA value. In that case, action qualifier unit cannot catch a matching between PWM counter and comparator. This results in sending wrong switching signals to IGBTs.

Second step is to reset the PWM counter. When PWM counter is reset in every tripzone interrupt, this condition makes the system to synchronize to the secondary current.

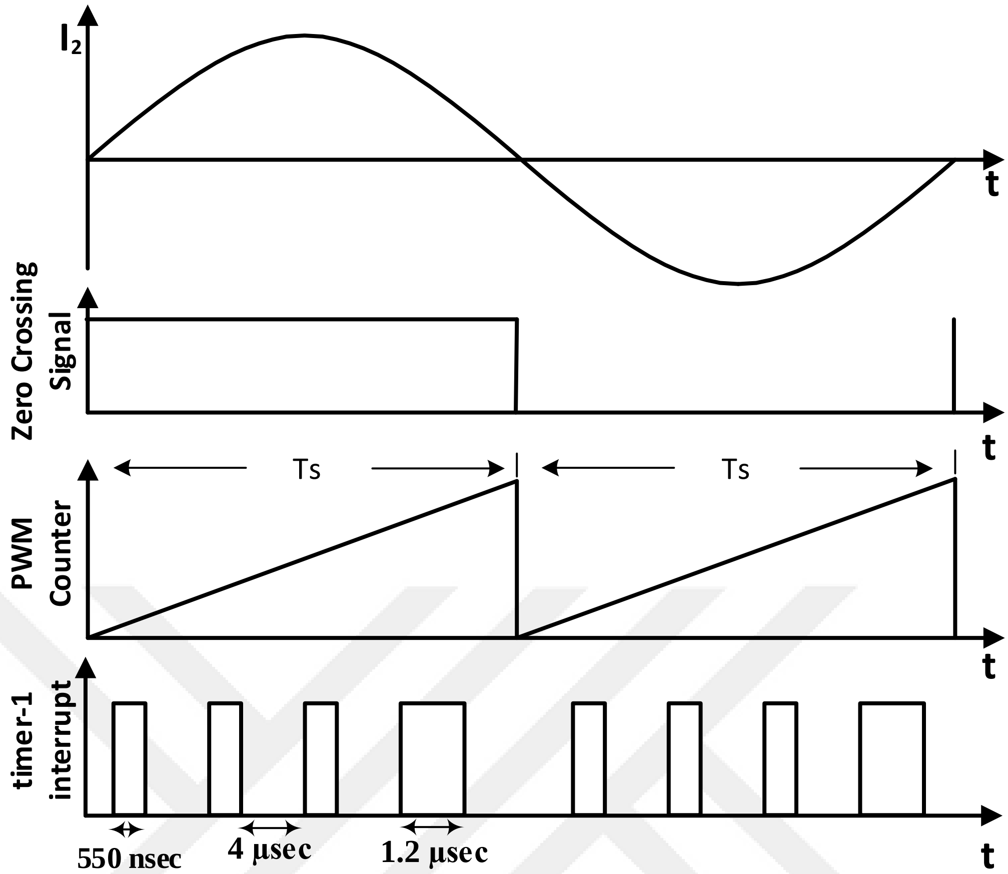

Figure 5.7 Timing diagram of timer-1 interrupt

After that, a timer value is read in order to obtain half period of secondary current, reloaded and restarted. When system generates an interrupt for each zero-crossing and these procedures are executed, timer value supplies half period of the secondery current. In order to generate an interrupt at the next zero-crossing moment, pre-determined digital comparator input condition is re-defined for the opposite level. A moving average filter (MAF) is used so as to smooth the change of half peripd velue. Finally, timer-1 interrupt is enabled in order to measure I_{dc} and apply PI controller.

When timer-1 interrupt is generated, battery current is read and conduction angle value is calculated. It is set in every 4 μsec in order to gather four data during half cycle as shown in Figure 5.7. Conversion in analog to digital converter unit of microcontroller gathers fourth current data and sums each data up. For the first three interrupt service routine, only current value is read. When fourth interrupt of a half

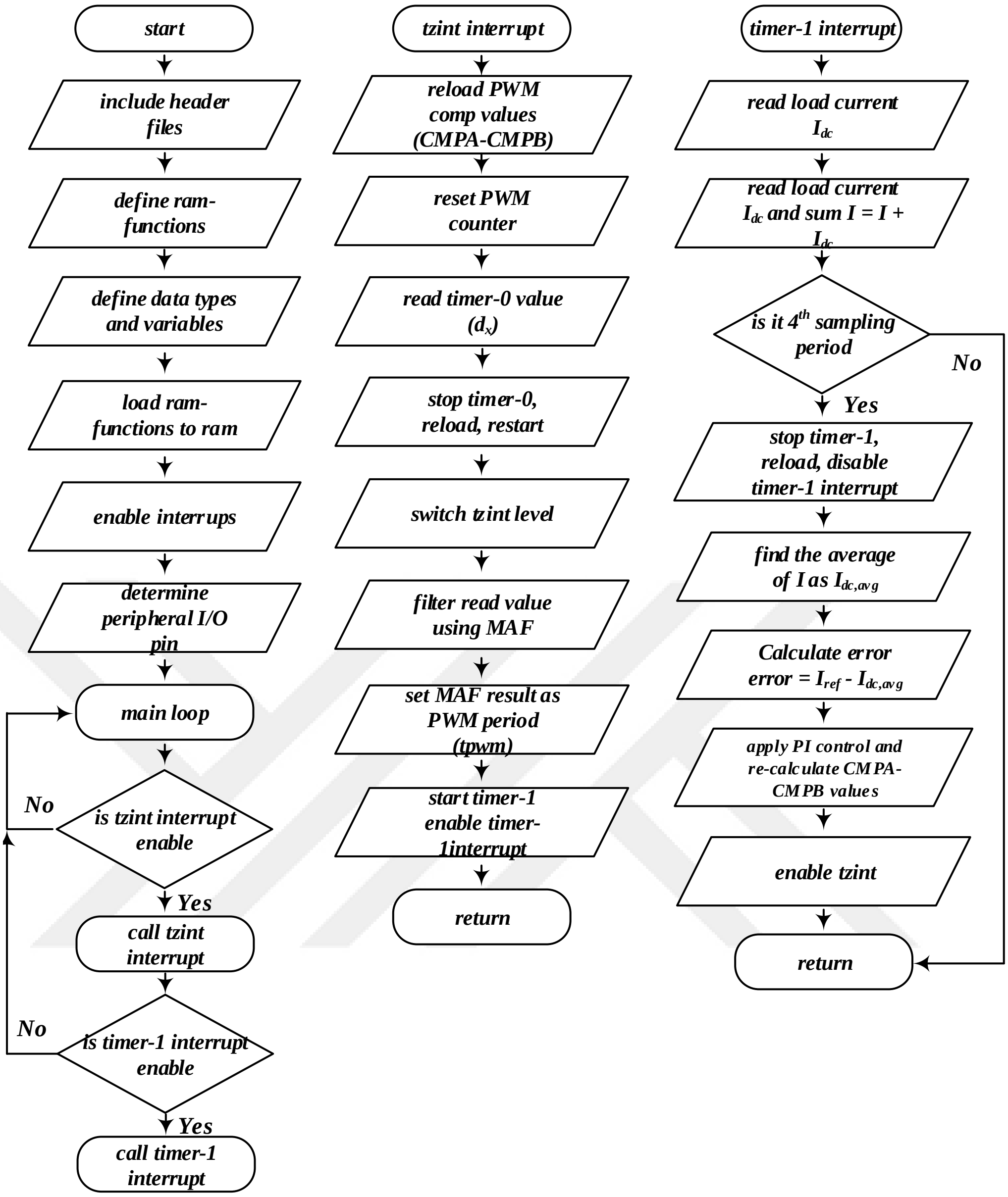

Figure 5.8 Flow chart of PLL logic and PI controller

cycle is generated, fourth sampled data is summed up with other three current data and average of the summation is calculated in order to obtain average charge current. Hence, the first three timer interrupt is shorter than fourth one. Timer-1 unit is reset and re-loaded at the end of the each interrupt service routine. In order to block wrong generated timer-1 interrupt, it is not enabled end of the fourth interrupt again. In the fourth timer interrupt, PI controller calculates the conduction angle value, values of CMPA and CMPB are re-calculated with respect to new conduction angle. Finally, tripzone interrupt is enabled. Figure 5.8 shows flowchart of the algorithm.

CHAPTER SIX

EXPERIMENTAL AND SIMULATION VERIFICATION

Designed system is tested in laboratory condition on a 2 kW IPT system prototype. The system is fed by a dc power supply which can provide 2kW output. Primary and secondary coils are designed identical and inductance values of them are 140 μH. They were winded 24 turns using solid round copper wire, outer diameter 400 mm. Coils are designed in order to obtain 0.2 coupling coefficient when the distance between them is 150mm (Tezcan et al., 2017). Primary side coil is connected to a full bridge inverter through a series 470 nF compensation capacitor. The secondary side coil is also compensated by a series 470 nF capacitor and its output is connected semi-bridgeless rectifier of which the topology is given in Chapter V. Secondary side rectifier circuit is run with purely resistive control method. Primary side is run in order to supply symmetrical square wave form as output voltage at constant frequency which is equal to 20.6 kHz. Output of the rectifier is filtered by an electrolytic 470 μF dc bus capacitor. The load is 96 V lead-acid battery package. The main part of the prototype system is shown in Figure 6.1.

In order to determine coil resistor and inductor values, test steps are as follows; circuit was run at 20.6 kHz, when secondary coil was open circuit. Using primary side voltage and current fundamental values, magnitude of the input impedance value was calculated. Primary current angle gives impedance angle. Coil inductance values were measured using a measurement device directly.

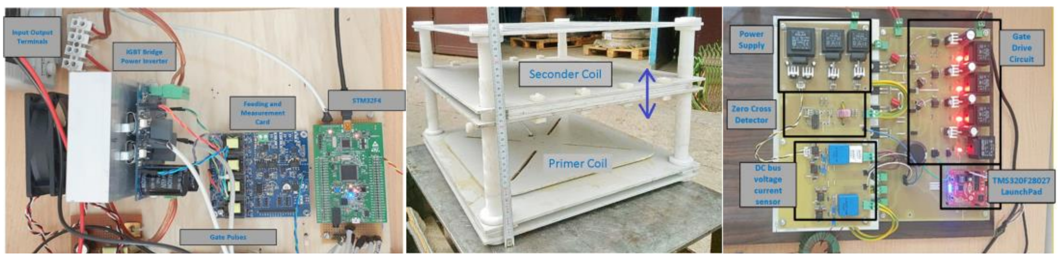

Figure 6.1 Prototype of the designed system a) Primary side inverter, IGBT driver circuits b) Primary and Secondary side coils and their mounted plate c) Secondary side rectifier, IGBT driver, zero-crossing and power supply circuits (Personal archive, 2017)

In order to calculate coupling coefficient between coils, the following steps are applied (Duarte & Felic, 2014);

Using equivalent circuit given in Figure 3.6, the following equations are written;

$$V_1 = j\omega(I_1 L_1 - M I_2) \tag{6.1}$$

$$V_2 = j\omega(M I_1 - L_2 I_2) \tag{6.2}$$

In order to formulate coupling coefficient, secondary side coil is shorted and secondary voltage is equal to zero. Hence, from equation (6.2);

$$I_2 = \frac{M I_1}{L_2} \tag{6.3}$$

If equation (6.3) is written in equation (6.1);

$$V_1 = j\omega I_1 \left(L_1 - M \frac{M}{L_2} \right) \tag{6.4}$$

And the inductance value that measured when secondary coil is shorted is;

$$L_s = L_1 - \frac{M^2}{L_2} \tag{6.5}$$

Therefore, coupling coefficient is calculated by re-arranging equation (6.5);

$$k = \frac{M}{\sqrt{L_1 L_2}} = \sqrt{1 - \frac{L_s}{L_1}} \tag{6.6}$$

Before designed circuit connected to the 2 kW IPT system, coils were measured at open circuit-short circuit conditions in order to calculate coupling coefficient for eight different distance values between the coils. Results are given in Table 6.1 (Boztepe, 2017);

Figure 6.2 illustrates generated signals, in other words timing diagram shown in Figure 5.2, with respect to secondary current. Zero-crossing detector circuit shown in Figure 5.3 generates zero-crossing signal according to zero crossing of secondary current. It can be observed in Figure 6.2, by timer-1 interrupt, battery charge current is sampled four times in a half cycle of secondary current. Moreover, as seen in the figure, secondary side current is switched in resistive mode successfully.

Table 6.1 Coupling Coefficient for 138 μ H at different distances between the coils

		Primary Coil			Secondary Coil		
Distance	Distance between coils (cm)	Open circuit self inductance (μ H)	Short circuit self inductance (μ H)	Coupling coefficient k= $\sqrt{1-\frac{L_s}{L_1}}$	Open circuit self inductance (μ H)	Short circuit self inductance (μ H)	Coupling coefficient k= $\sqrt{1-\frac{L_s}{L_1}}$
1	3.8	136.1	78.2	0.652	136.5	79.5	0.646
2	6.3	136.3	104.2	0.485	137	104.7	0.486
3	8.8	136.6	118.3	0.365	137.5	119	0.367
4	11.3	136.7	126	0.280	138	127.2	0.280
5	13.7	136.8	130.2	0.219	138.3	131.5	0.221
6	16.1	137	132.8	0.174	138.1	133.9	0.174
7	18.6	136.8	134.2	0.138	138.2	135.7	0.135
8	21.2	136.9	135.3	0.108	138.3	136.6	0.111

Figure 6.3 shows secondary side voltage and current wave forms at 16 Ω resistive load. System operating frequency is 20.6 kHz, coupling coefficient is 0.45. In the experiment, charge current reference value was set from 2A to 6A in 2A steps while PI controller was being run. For 6A charge current, system input voltage was increased because of low input power condition. Load voltage depends on the charge current.

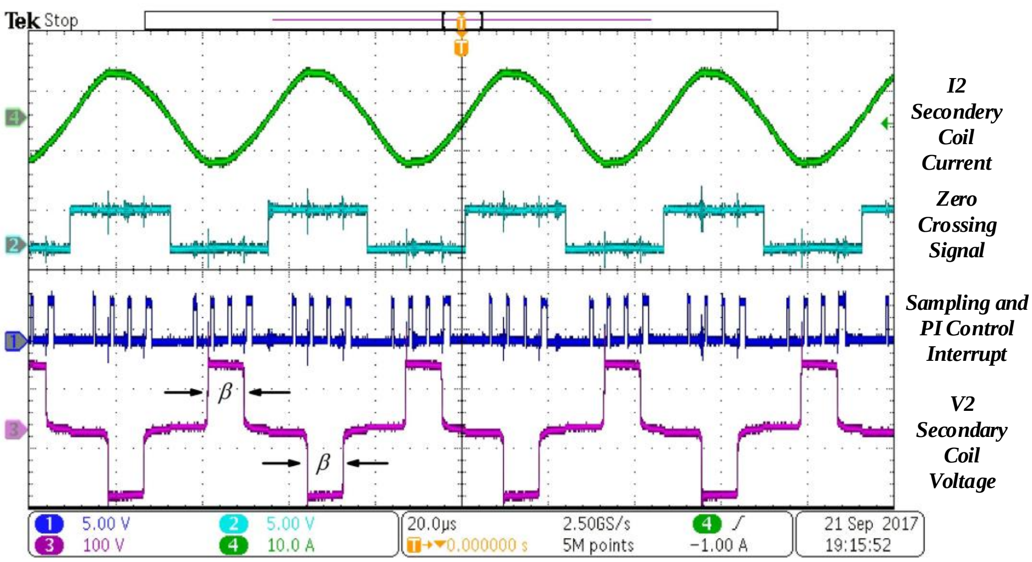

Figure 6.2 Observed oscilloscope waveforms of the zero-crossing, timer-1 interrupt and timing signals

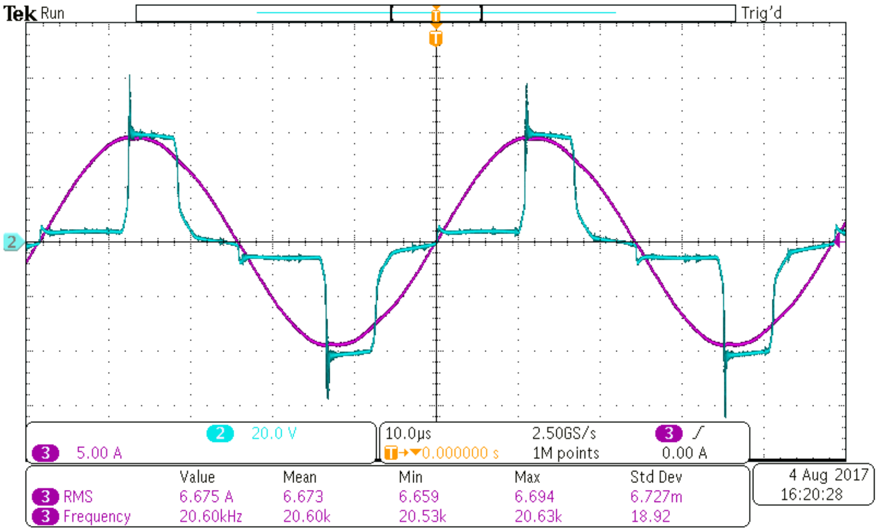

(a)

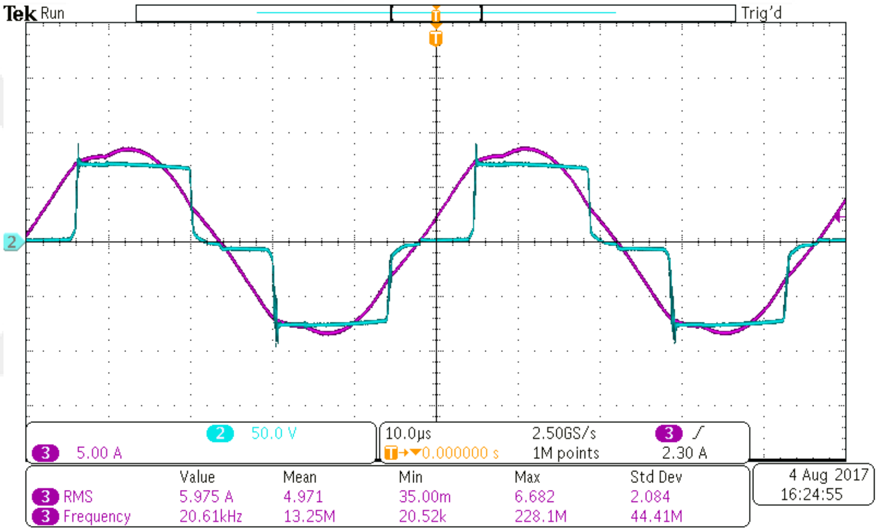

(b)

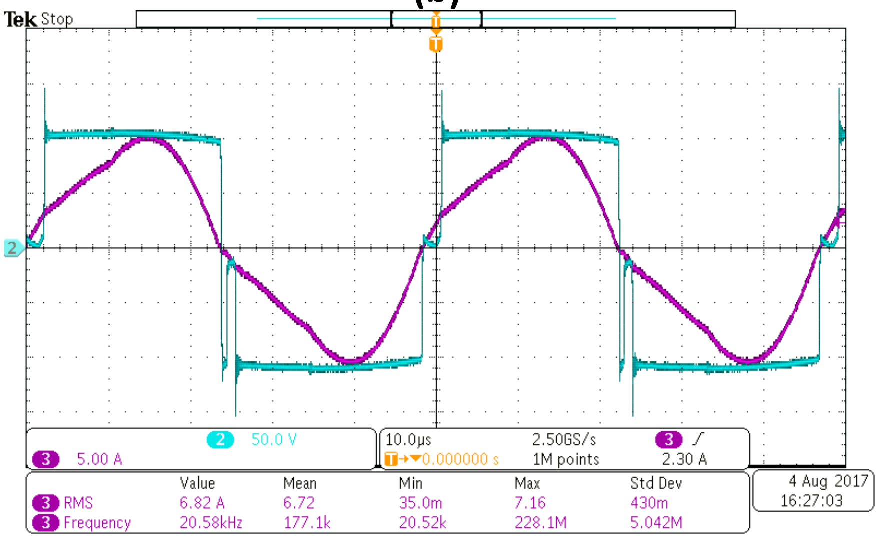

(c)

Figure 6.3 Secondary side voltage and current waveforms at resistive load condition R_{dc}= 16 Ω a) V_{in} = 60 V, I_{out} = 2 A b) V_{in} = 60 V, I_{out} = 4 A c) V_{in} = 70 V, I_{out} = 6 A

When charge current is increased, output voltage is increased, since load type used in experiment is resistive and its value was kept constant. It can be seen in the figure that secondary side voltage value is dependent on load current (Gürbüz et al., 2017).

Figure 6.4 (a) illustrates close loop response of the controller while reference value is being changed from 0 A to 6 A in 2A steps. The results are obtained at battery load condition and operating frequency is equal to 20.6 kHz. Coupling coefficient between coils is 0.45. In order to prevent direct connection between battery and the dc bus capacitor, a diode is connected between them. While current is not flowing toward battery, this diode is reverse-biased. Hence, on that interval, battery voltage is seen as zero volt as shown in Figure 6.4 (a). In Figure 6.4 (b), current step responses are given

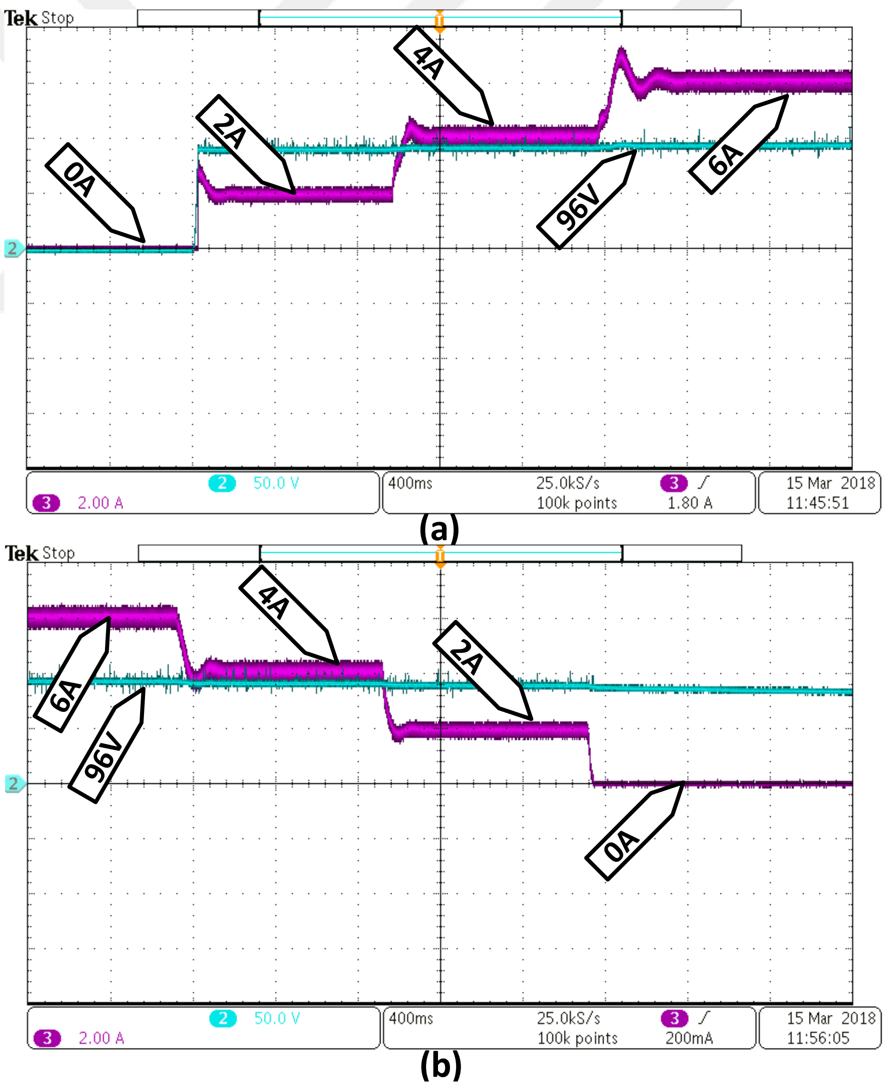

Figure 6.4 Closed loop control step responses with battery load a) from 0A to 6A b) from 6A to 0A

for decreasing reference values. When current is zero, a voltage value is seen because of the charged dc bus capacitor.

Table 6.2 Efficiency results for the inverter circuit

Degree	$\eta_{analysis}(\%)$	$\eta_{simulation}(\%)$	$\eta_{experiment}(\%)$
30^0	96.71	99.54	88
60^0	96.44	98.07	96.6
90^0	96.12	96.76	93.6
120^0	95.84	95.71	93.6
150^0	95.67	94.9	96.5
180^0	95.61	94.74	94.1

Table 6.3 Efficiency results for the coil circuit

Degree	$\eta_{analysis}(\%)$	$\eta_{simulation}(\%)$	$\eta_{experiment}(\%)$
30^0	90.23	90.23	92.8
60^0	92.63	92.63	94.8
90^0	92.94	92.94	94.5
120^0	92.77	92.77	94
150^0	92.56	92.56	95.1
180^0	92.47	92.47	94.8

Table 6.4 Efficiency results for the rectifier circuit

Degree	$\eta_{analysis}(\%)$	$\eta_{simulation}(\%)$	$\eta_{experiment}(\%)$
30^0	82.62	81.47	74.6
60^0	89.98	89.68	83.8
90^0	92.69	93.47	87.1
120^0	94.05	94.7	91.8
150^0	94.81	95.75	90.9
180^0	95.23	96	90.9

Experiment for efficiency analysis was made at 96 V battery load condition. The system was run at open loop control, input voltage was adjusted to 75 V. Operating

Table 6.5 Overall efficiency of the system

Degree	$\eta_{analysis}(\%)$	$\eta_{simulation}(\%)$	$\eta_{experiment}(\%)$
30^0	72.1	72.9	60.9
60^0	80.38	81.44	76.7
90^0	82.8	84.07	77.1
120^0	83.62	84.07	80.5
150^0	83.95	84	83.4
180^0	84.19	83.95	81.1

frequency is 20.6 kHz, coupling coefficient of the coils was set as 0.45. In order to estimate efficiency of the circuits and overall system, piecewise linear model which is spoken of in Chapter IV is used for IGBT and diode switches in both simulation model and analysis. In the mathematical analysis of system efficiency, fundamental analysis method is used. Analysis model calculation starts with conduction angle definition and after that an iterative calculation is made until defined input voltage condition is supplied. Battery load is modelled with a constant voltage value. The simulation model of the system is run at MATLAB/Simulink. However, IGBT model in Simulink does not include switching loss model. Therefore, switching losses are not included in simulation model. In Table 6.2, Table 6.3, Table 6.4, Table 6.5 efficiency results are given for the system circuits and for overall. At low conduction angle values, it has

Table 6.6 Input-Output Power results

	P_{in}			P_{out}		
Degree	$P_{analysis}$ (watt)	$P_{simulation}$ (watt)	$P_{experiment}$ (watt)	$P_{analysis}$ (watt)	$P_{simulation}$ (watt)	$P_{experiment}$ (watt)
30^0	255	237	284	183.8	172.8	173
60^0	432.4	412.2	437	347.5	335.7	335
90^0	580.3	559.5	597	480.5	470.4	460
120^0	690	683.8	712	577	574.8	573
150^0	756.3	772.5	767	634.9	649	640
180^0	777.2	814	863	654.4	683.4	700

been mentioned that secondary current increases. This results in decreasing of primary current. Hence, as seen in Table 6.2, inverter efficiency is higher at low conduction angle values. All experimental results are together with the analysed and simulated efficiency results.. In experimental results, efficiency results are less then analysis and simulation results.

Table 6.6 shows input-output power relation with β and experiment results are in agreement with analysis and simulation results, from Figure 6.5 to 6.10, voltage and current wave forms are illustrated for both primary and secondary side. It is seen that simulation and experimental results are in agreement.

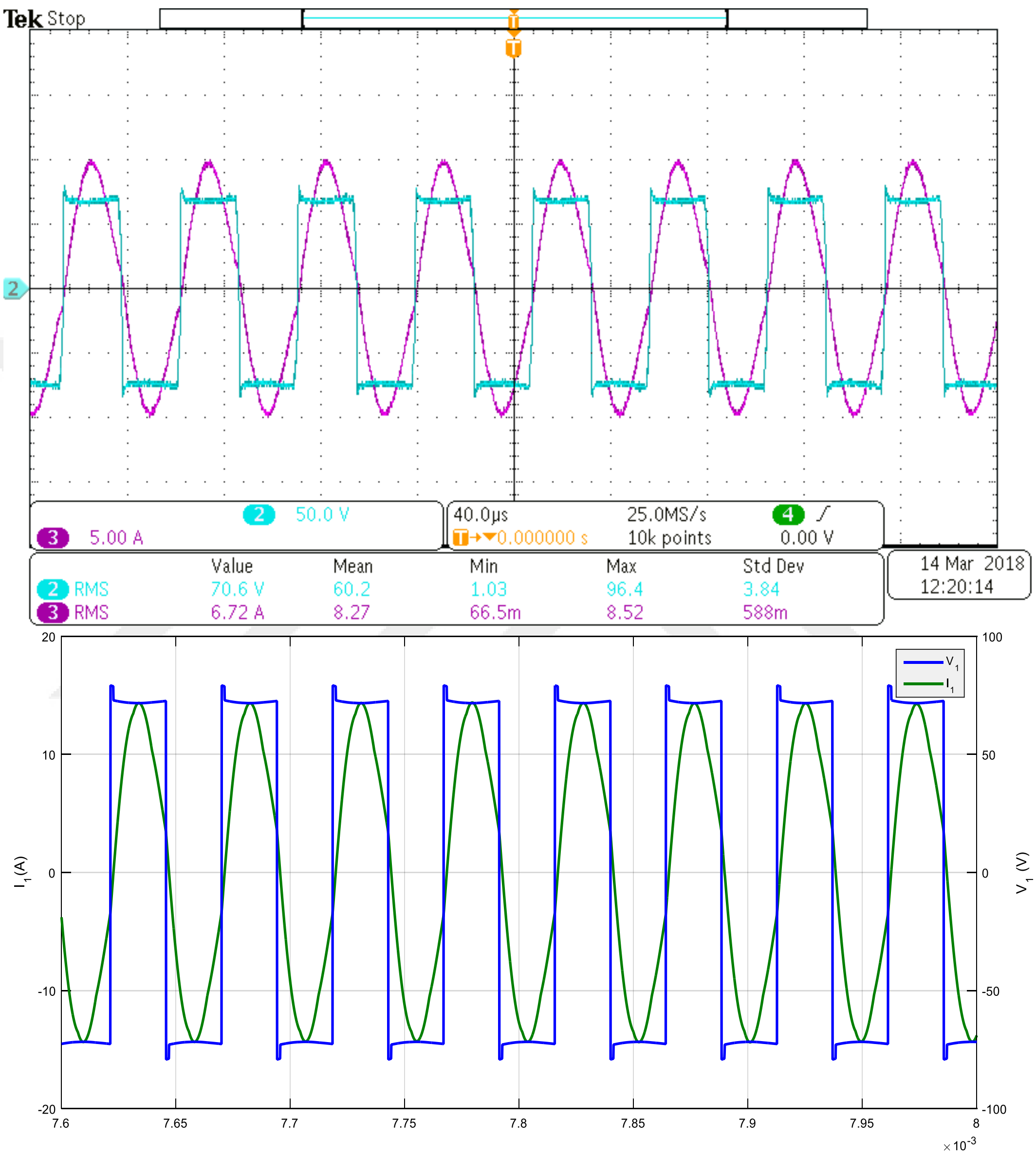

Figure 6.5 Simulation and experimental voltage-current results for primary side waveforms for $\beta = 60^0$ with battery load

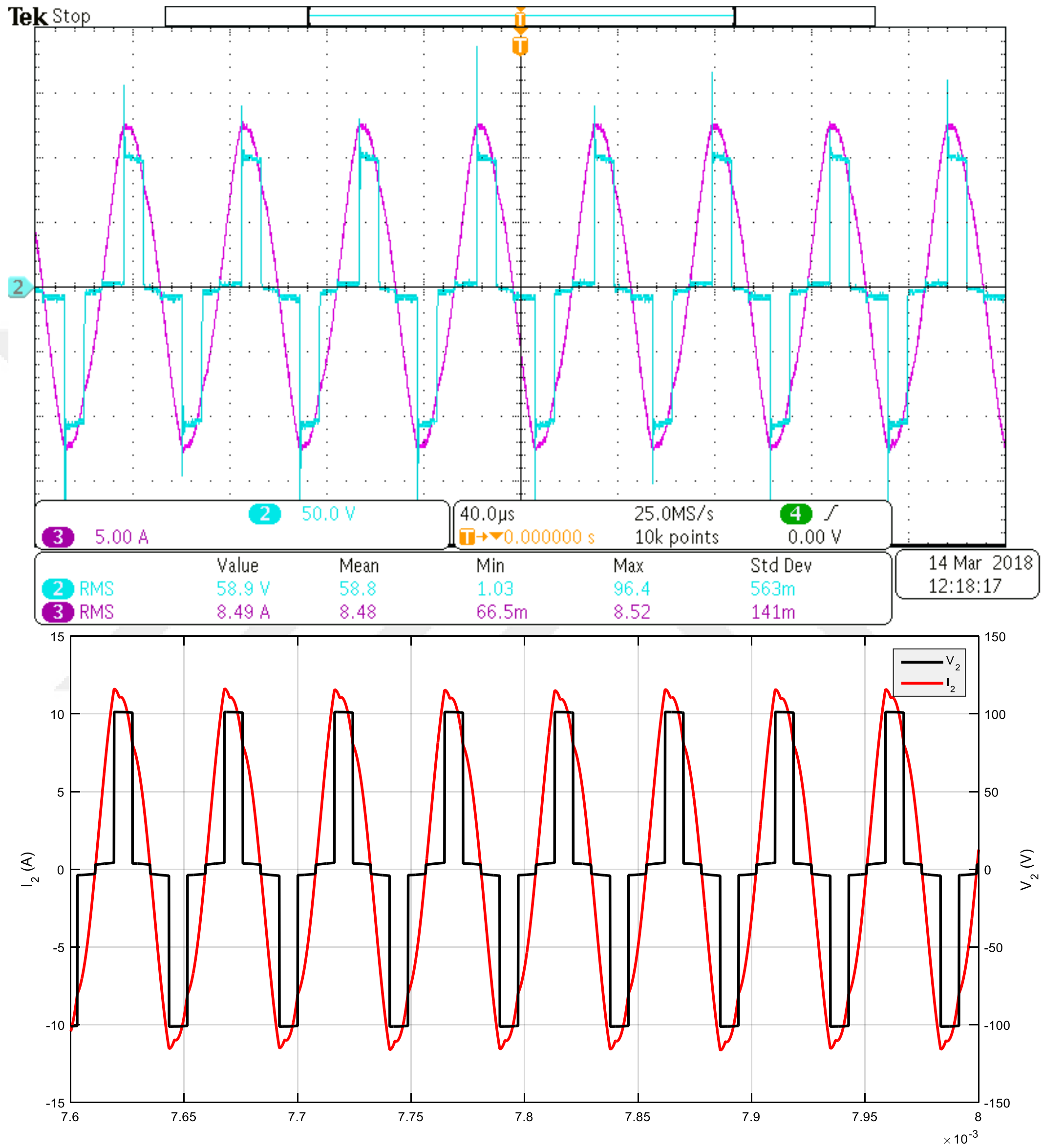

Figure 6.6 Simulation and experimental voltage-current results for secondary side waveforms for β = 60^0 with battery load

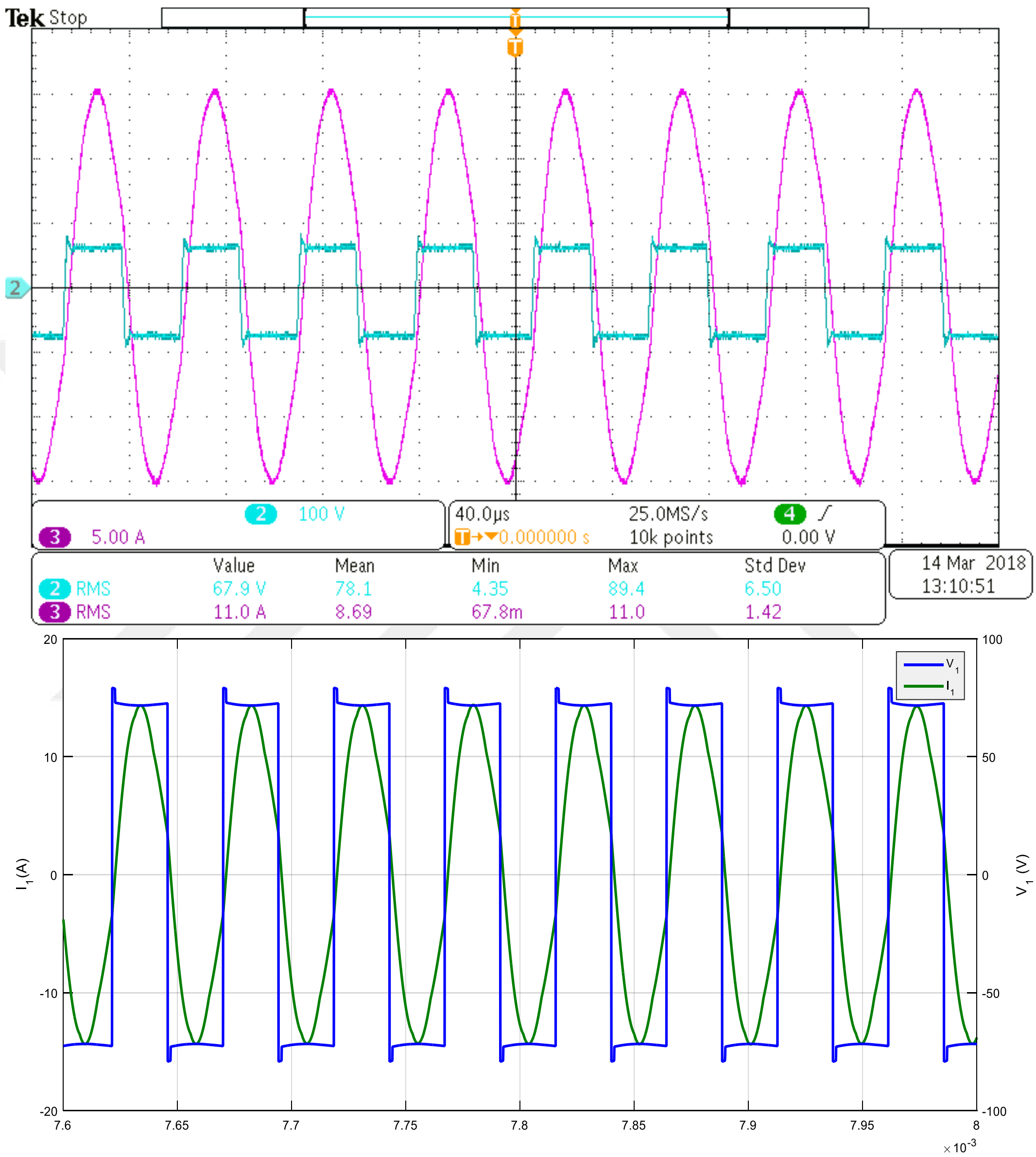

Figure 6.7 Simulation (lower side) and experimental (upper side) voltage-current results for primary side waveforms for $\beta = 120^0$ with battery load

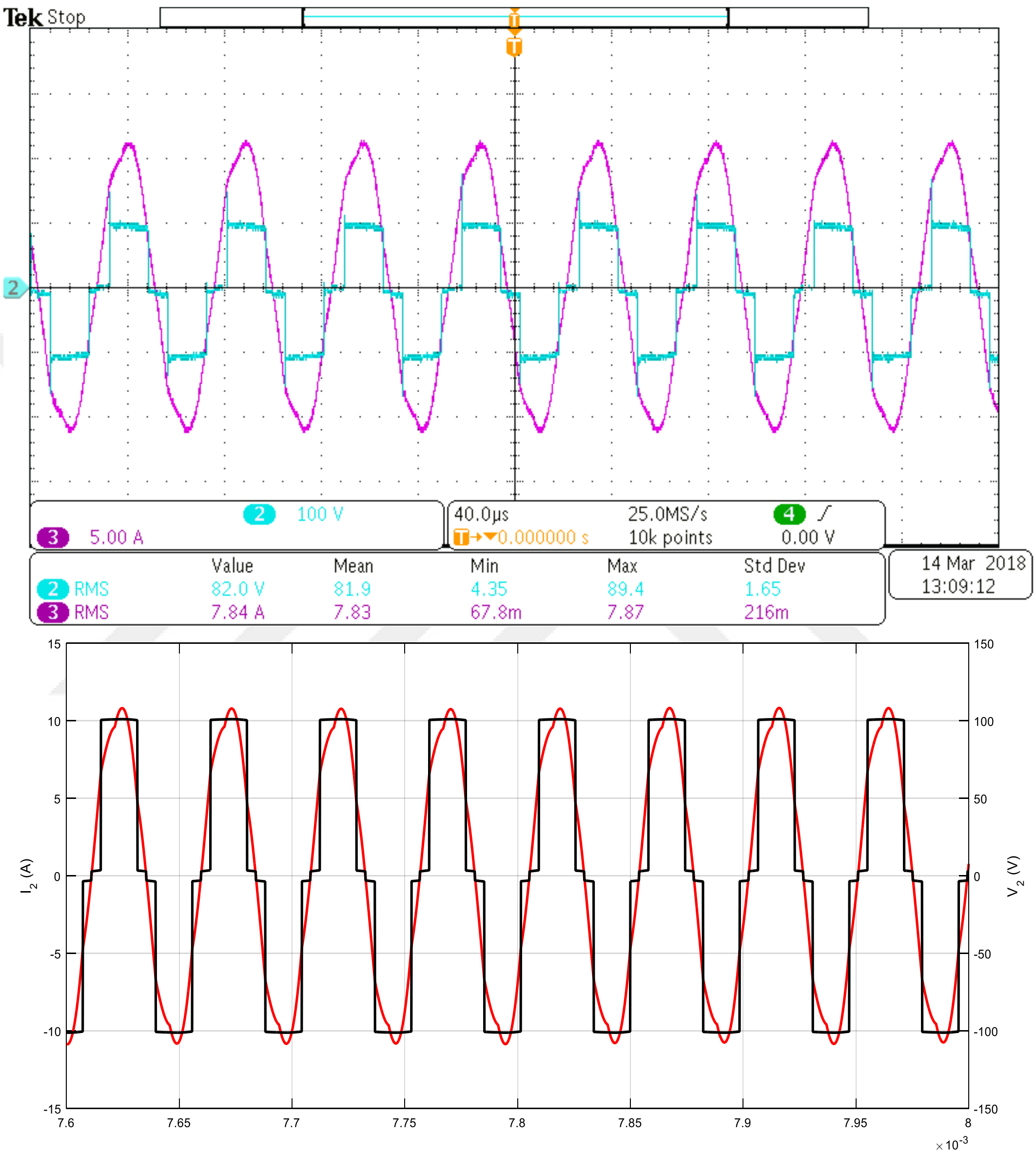

Figure 6.8 Simulation (lower side) and experimental (upper side) voltage-current results for secondary side waveforms for β = 120^0 with battery load

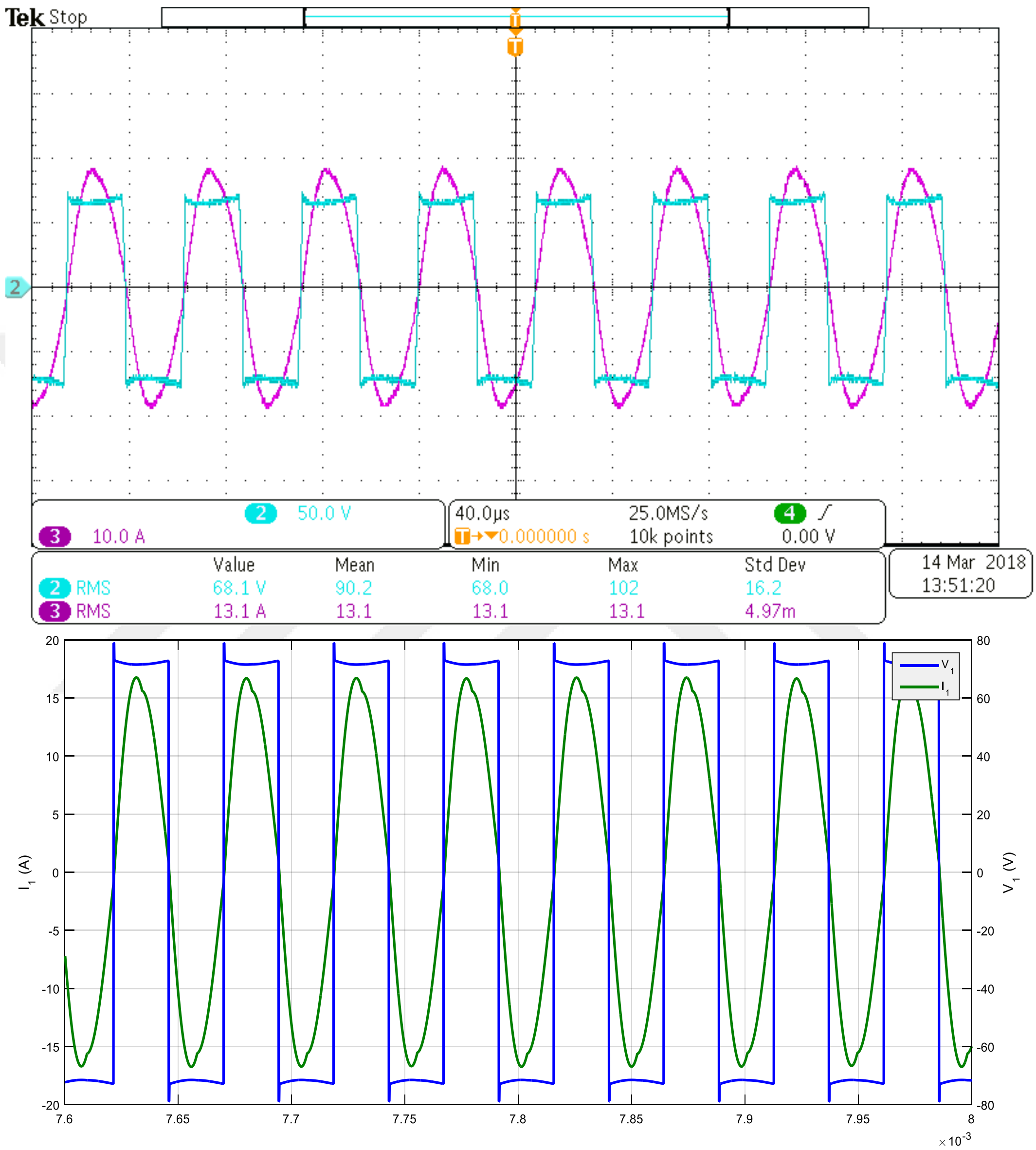

Figure 6.9 Simulation (lower side) and experimental voltage-current results for primary side waveforms for $\beta = 180^0$ with battery load

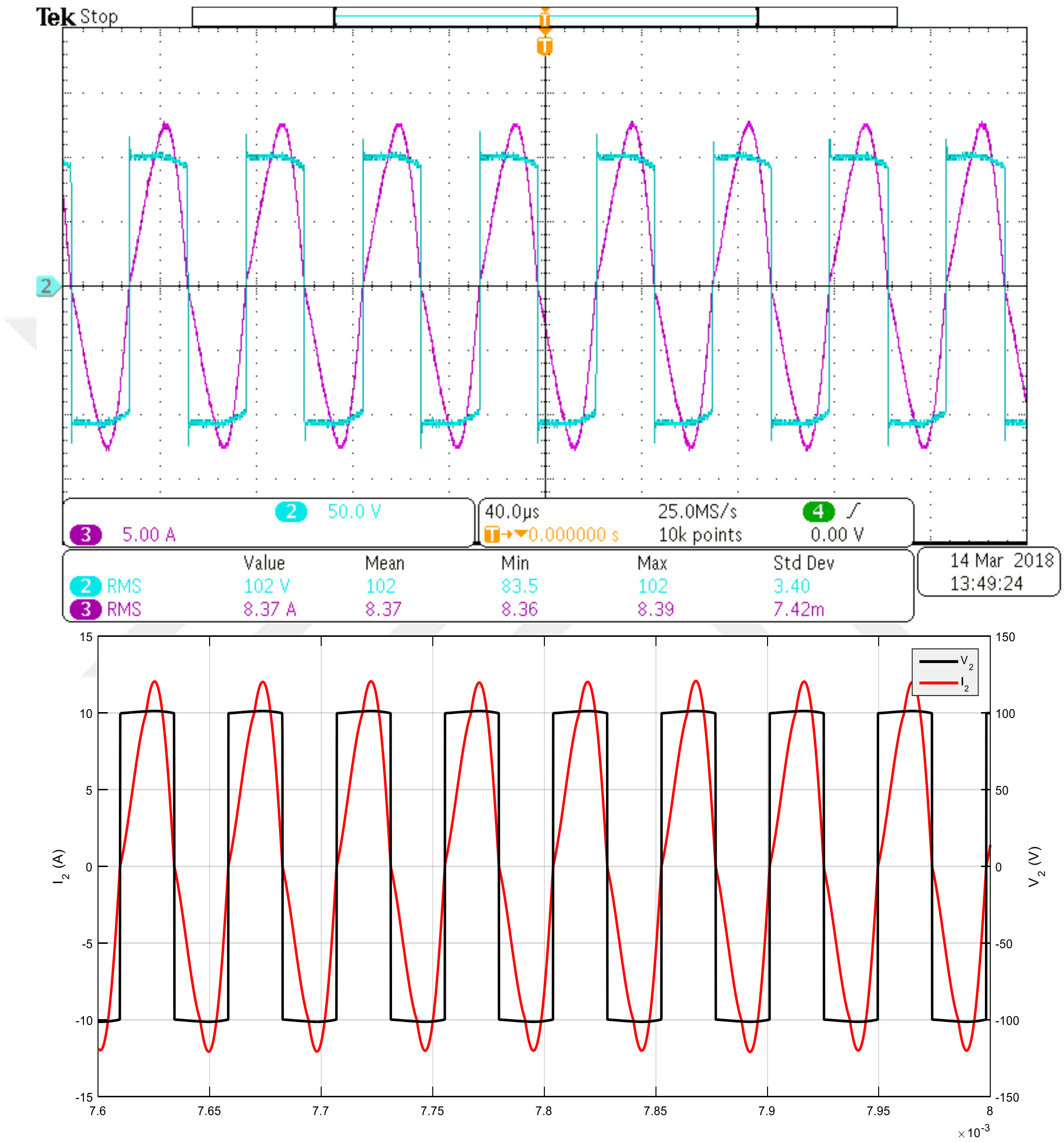

Figure 6.10 Simulation (lower side) and experimental voltage-current results for secondary side waveforms for β = 180^0 with battery load

CHAPTER SEVEN
CONCLUSION

In this study, a secondary side control method for IPT system is proposed. The method is based on control of the load resistively. In other words, the method adjusts apparent load at rectifier input terminals so that the load can draw desired charge current and does not draw reactive power. The control topology is chosen as semi-bridgeless active rectifier in order to decrease number of switching components and losses. The chosen topology and its working modes are examined. Besides, control methods used in this topology are expressed. The load characters of the circuit have been investigated under purely resistive control and phase shift control.

According to circuit modelling, mathematical analysis of the model is made. In order to make analysis of the control method, coils are modelled as air cored, loosely coupled transformer. Voltage and current gains, efficiency analyses have been investigated in terms of load and operating frequency. The maximum efficiency point is equal to the point where voltage and current gains are equal to each other.

According to input-output voltages and conduction angle, efficiency analysis method has been investigated by calculating load value. The analysis method is based on an iterative solution. The calculation applies iteration until input voltage is equal to desired value. Moreover, primary side, secondary side and dual side control types have been analysed. After that, effects of all control types on coil efficiency have been compared with each other in a few different voltage gain conditions. According to calculations, dual side control has better performance at partial load conditions. On the other hand, control angles can limit the charge current with respect to input and output voltage ratio.

The next step, system conduction and switching losses have been investigated. At secondary side, switching strategy is based on hard switching owing to resistive load control. Therefore, switching and conduction losses at secondary side depend on conduction angle β. Moreover, it can be seen in the analysis that conduction angle affects primary side losses implicitly. Because apparent load has effect on input impedance angle of overall system. This situation results in increasing average current passing through anti-parallel diodes. Hence, primary side losses increase because of higher voltage drop on diodes.

The control logic has been implemented using TMS320F28027 card. Controller has been designed as PI controller and experimental results have been obtained under resistive and battery load conditions. In order to realize resistive control on secondary side active rectifier, half cycle of secondary current is detected using a timer which is reset when each zero-crossing signal is detected. Furthermore, zero-crossing signal is used so as to reset PWM counter and lock on the phase of secondary current. In order to reduce delay between real and sensed secondary current, current transformer is used at zero-crossing detector circuit. Finally, experimental setup was built and tested succesfully. Experimental results are observed to be in agreement with analyses and simulation results. It can be observed in Table 6.5, experimental results are different about 10% from analysis and simulation results at low conduction angles, whereas experimental efficiency results at the higher conduction angle value are quite close to analysis and simulation results with 3% difference.

REFERENCES

Berger, A., Agostinelli, M., Vesti, S., A., O. J., Cobos, J. A., & Huemer, M. (2015). A wireless charging system applying phase shift and amplitude control to maximize efficiency and extractable power. *IEEE Transactions on Power Electronics*, *30*(11), 6338–6348.

Bertoluzzo, M., Jha, R. K., & Buja, G. (2015). Series-series resonant IPT system analysis under frequency mismatch. *41st Annual Conference of IEEE Industrial Electronics Society*, 439–444.

Bojarski, M., Asa, E., & D, C. (2014). ffect of wireless power link load resistance on the efficiency of the energy transfer. *IEEE International Electric Vehicle Conference*, 1–7.

Bosshard, R., Kolar, J. W., & B., W. (2014). Control method for inductive power transfer with high partial-load efficiency and resonance tracking. *International Power Electronic Conference*, 2167–2174.

Boztepe, M. (2017). Elektrikli Araçlar için Temassız bir Şarj Sistemi Tasarımı ve Optimizasyonu (Technical Report). *The Scientific and Technological Research Council of Turkey (TÜBİTAK) Project no: 115E116.*

Chen, X., Shenghua, H., Bingzhang, L., & X, Y. (2016). Thermal calculation of IGBT, FWD in PWM inverter for electric engineering maintenance rolling stock. *9th International Conference on Electrical Machines and Systems*, 1–5.

Chung, E., Lim, G. C., Ha, J., Ha, J. I., & Y., K. K. (2017). Output voltage control for series-Series compensated wireless power transfer system without direct feedback from measurement or communication. *IEEE Energy Conversion Congress and Exposion*, 4035–4040.

Colak, K., Asa, E., Bojarski, M., Czarkowski, D., & Omar, O. C. (2015a). A novel phase shift control of semibridgeless active rectifier for wireless power transfer. *IEEE Transactions on Power Electronics*, *30*(11), 6288–6297.

Colak, K., Bojarski, M., Asa, E., & Czarkowski, D. (2015b). A constant resistance analysis and control of cascaded buck and boost converter for wireless EV chargers. *IEEE Applied Power Electronics Conference and Exposition*, 3157–3161.

Diekhans, T., & De Doncker, R. W. (2015). A dual-side controlled inductive power transfer system optimized for large coupling factor variations and partial load. *IEEE Transactions on Power Electronics*, *10*(11), 6320–6328.

Duarte, R. M., & Felic, G. K. (2014). Analysis of the Coupling Coefficient in Inductive Energy Transfer Systems. *Active and Passive Electronic Components*, *2014*, 6, Retrieved:July, 8,2018, from https://www.hindawi.com/journals/apec/2014/951624/.

Erickson, R., & Maksimovic, D. (2001). *Fumdamentals of Power Electronics*. Plenum Publisher.

Farzaneh, A., & Nazarzadeh, J. (2009). Precise loss calculation in cascaded multilevel inverters. *nternational Conference on Computer and Electrical Engineering*, 563–568.

Geng, Y., Yang, Z., & Lin, F. (2016). Optimization of dual side control strategy for wireless power transfer system in light rail vehicle. *IEEE PELS Workshop on Emerging Technologies:Wireless Power Transfer*, 54–59.

Gürbüz, F., Sürgevil, T., & Boztepe, M. (2017). Analysis, Design of a Secondary-Side Controlled Active Rectifier for Wire-less Battery Charging Application. *International Conference on Electrical and Electronics Engineering (ELECO)*, 406–410.

Hata, K., Imura, T., & Y, H. (2017). Maximum efficiency control of wireless power transfer system with half active rectifier based on primary current measurement. *IEEE 3rd International Future Energy Electronics Conference and ECCE Asia*, 1–6.

Kato, M., Imura, T., & Hori, Y. (2013). Study on maximize efficiency by secondary side control using DC-DC converter in wireless power transfer via magnetic resonant coupling. *World Electrical Vehicle Symposium*, 1–5.

Kazmierkowski, M. P., & Moradewicz, A. J. (2012). Unplugged but connected: Review of contactless energy transfer systems. *IEEE Industrial Electronics Magazine*, *6*(4), 47–55.

Kolar, J., Zach, F. C., & F., C. (1995). Losses in PWM Inverters Using IGBTs. *Electric Power Applications*, *142*(4), 285–288.

Krishan, S., Bhuyan, S., Kumar, V. P., Wang, W., Afif, J. A., & Lim, K. S. (2012). Frequency Agile Resonance-Based Wireless Charging System for Electric Vehicles. *IEEE International Electric Vehicle Conference*, 1–4.

Li, S., & Mi, C. C. (2015). Wireless power transfer for electric vehicle applications. *IEEE Journal of Emerging and Selected Topics in Power Electronic*, *3, 1*, 4–17.

Liu, X., Wang, T., Yang, X., Jin, N., & H., T. (2017). Analysis and design of a wireless power transfer system with dual active bridges. *Energies*, *10*(10), 1588–1608, from http://mdpi.com.

Mai, R., Liu, Y., Li, Y., Yue, P., G., C., & Z., H. (2017). An active rectifier based maximum efficiency tracking method using an additional measurement coil for wireless power transfer. *IEEE Transaction on Power Electronics*, *33*(1), 716–728.

Surgevil, T. (2004). Modeling and Simulation of Wind Energy Conversion System Using PWM Converters. *Graduate School of Natural and Applied Sciences of Dokuz Eylül University*.

Tezcan, Y., Ünal, H., Sürgevil, T., & M., B. (2017). Optimum coil design considering skin and proximity effects for a wireless battery charger of electric vehicle. *World Electromobility Conference*, 1–5.

Zhao, C., Wang, Z., Du, J., Wu, J., Zong, S., & X, H. (2014). Active resonance wireless power transfer system using phase shift control strategy. *IEEE Applied Power Electronics Conference and Exposition*, 1336–1341.

APPENDIXES

1.1 Appendix A

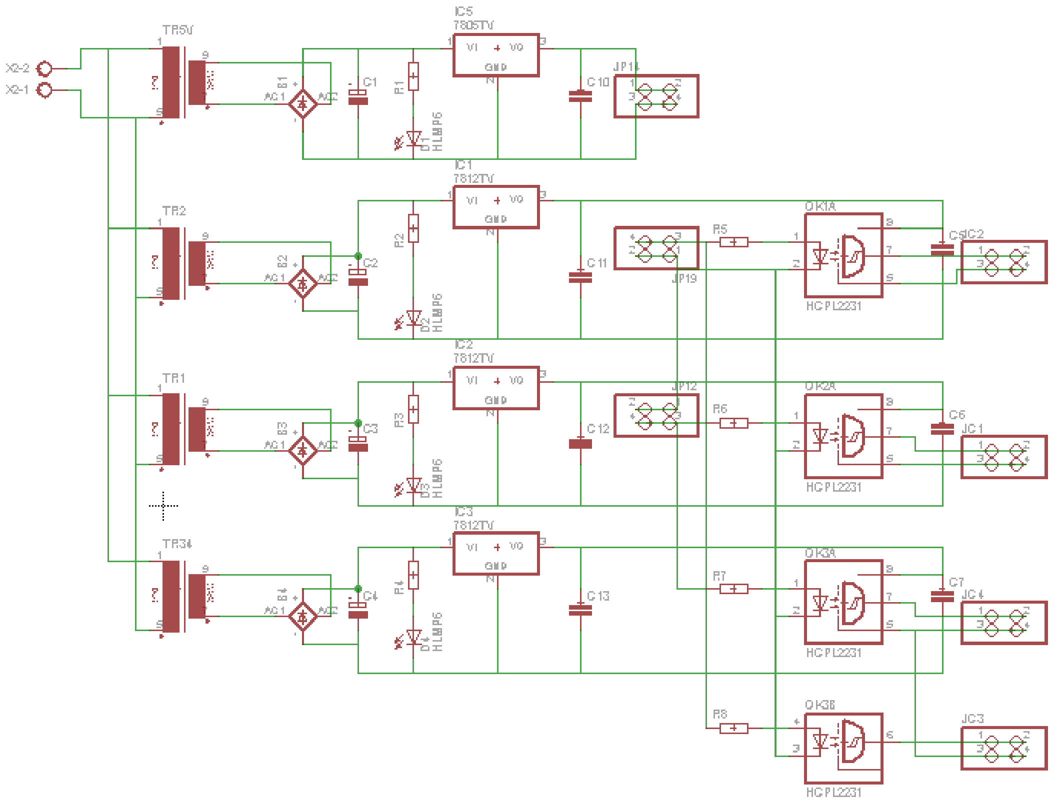

Figure A1.1 PWM Gate driving circuit

Schematic drawing of this circuit is in power_receiver(22.03.2017)_2.sch file and board drawing of it is in power_receiver(22.03.2017)_2.brd file as implemented with main board.

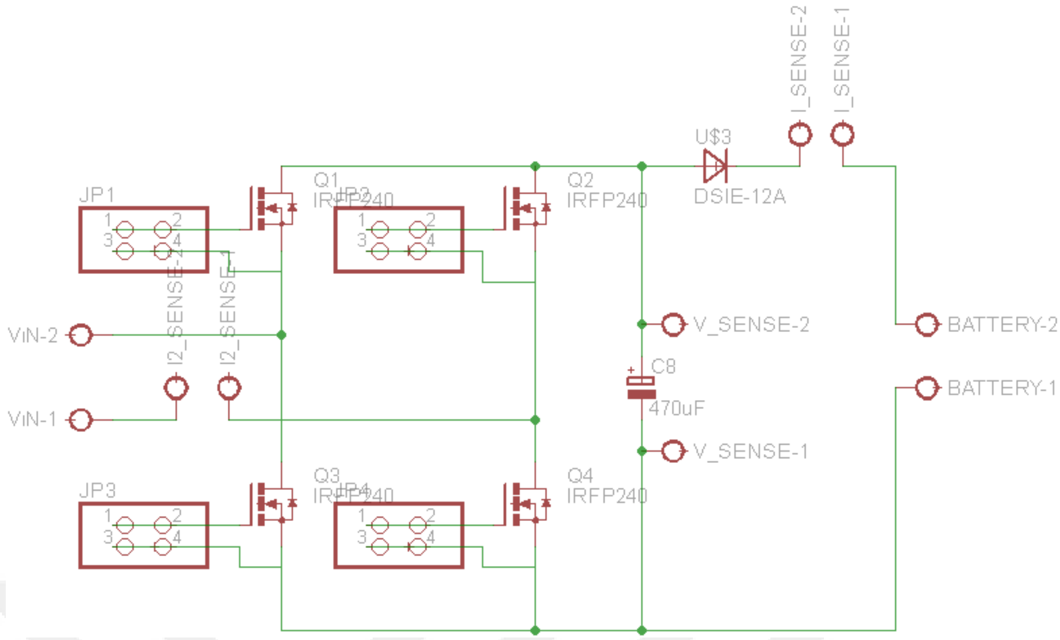

Figure A1.2 Secondary side rectifier circuit

Schematic drawing of this circuit is in power_receiver(22.03.2017)_2.sch file and board drawing of it is in power_receiver(22.03.2017)_2.brd file as implemented with main board.

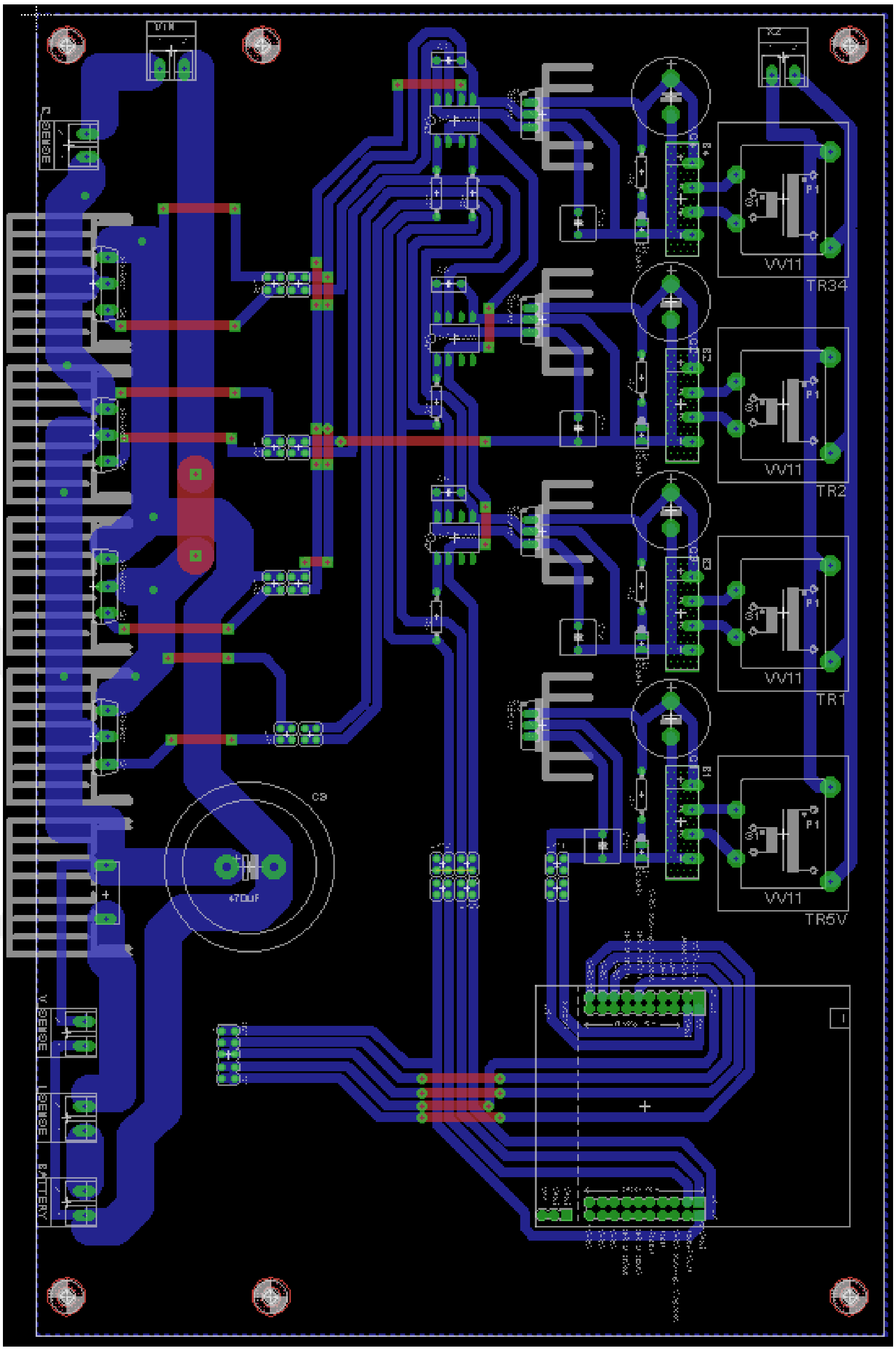

Figure A1.3 Secondary side rectifier&gate driving circuit

Schematic drawing of this circuit is in power_receiver(22.03.2017)_2.sch file and board drawing of it is in power_receiver(22.03.2017)_2.brd file as implemented with main board.

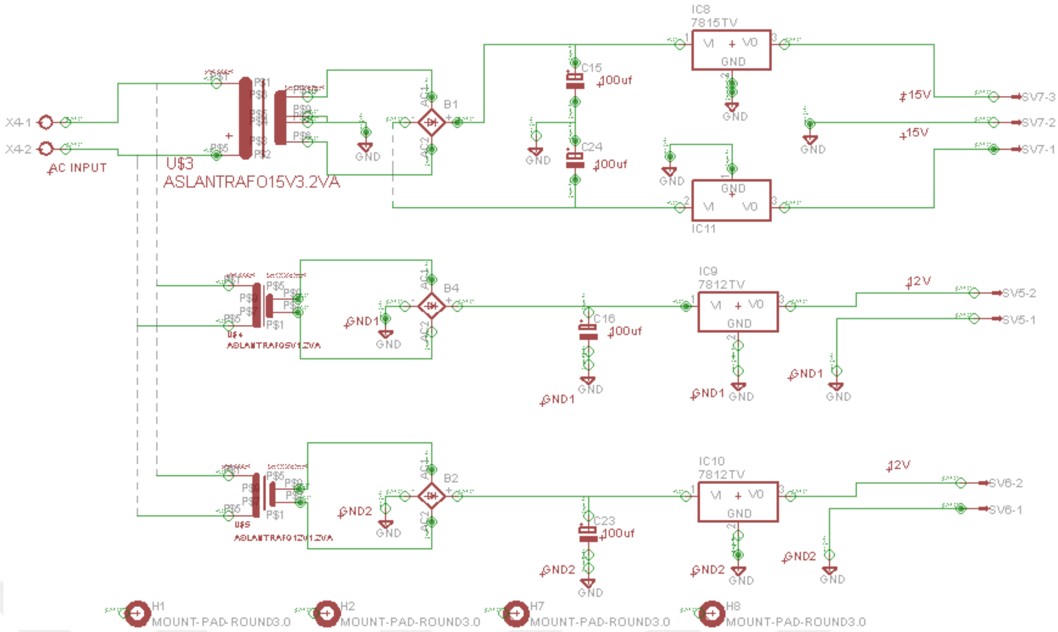

Figure A1.4 Power supply circuit

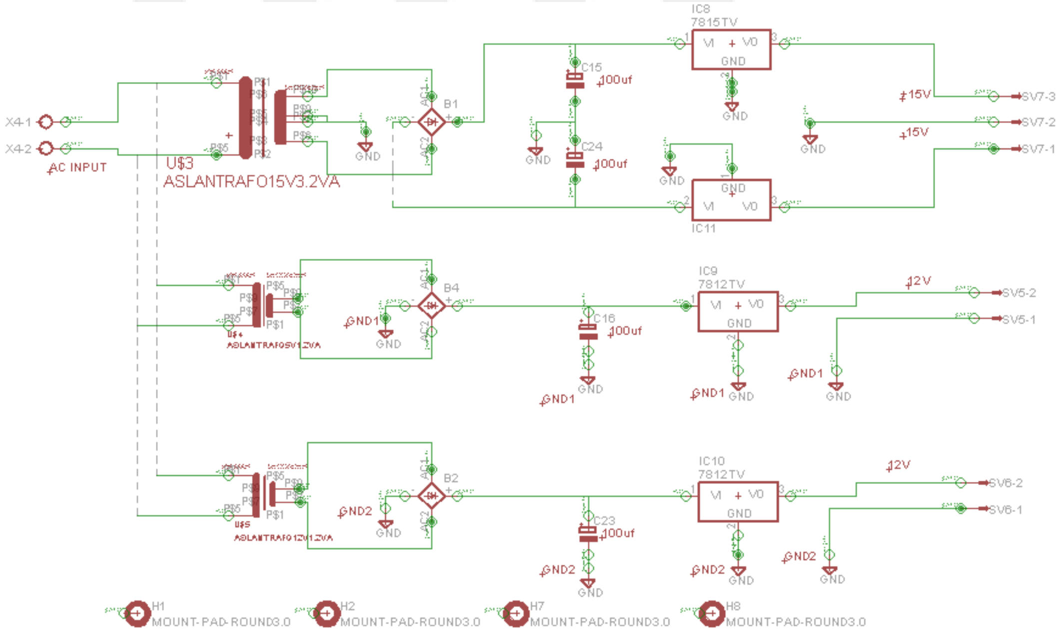

Figure A1.5 Voltage and current measurement circuit

Schematic drawing of these circuit are in sensor+zero_crossing+power(11.09.2017).sch file and board drawing of them is in sensor+zero_crossing+power(11.09.2017).brd file.

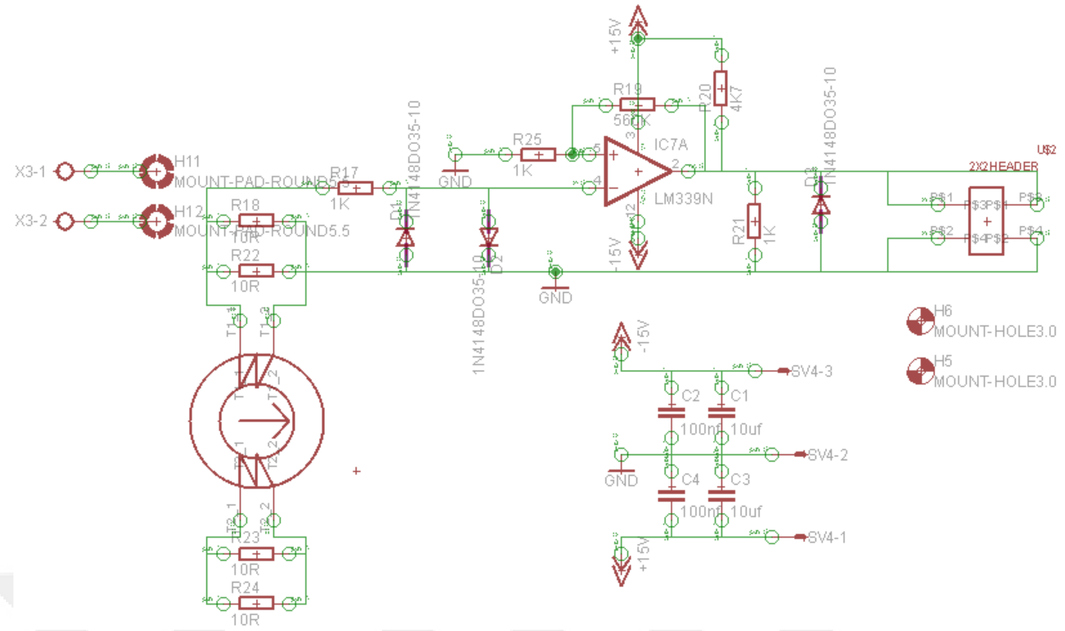

Figure A1.6 Zero crossing detector circuit

Schematic drawing of this circuit is in sensor+zero_crossing+power(11.09.2017).sch file and board drawing of it is in sensor+zero_crossing+power(11.09.2017).brd file.

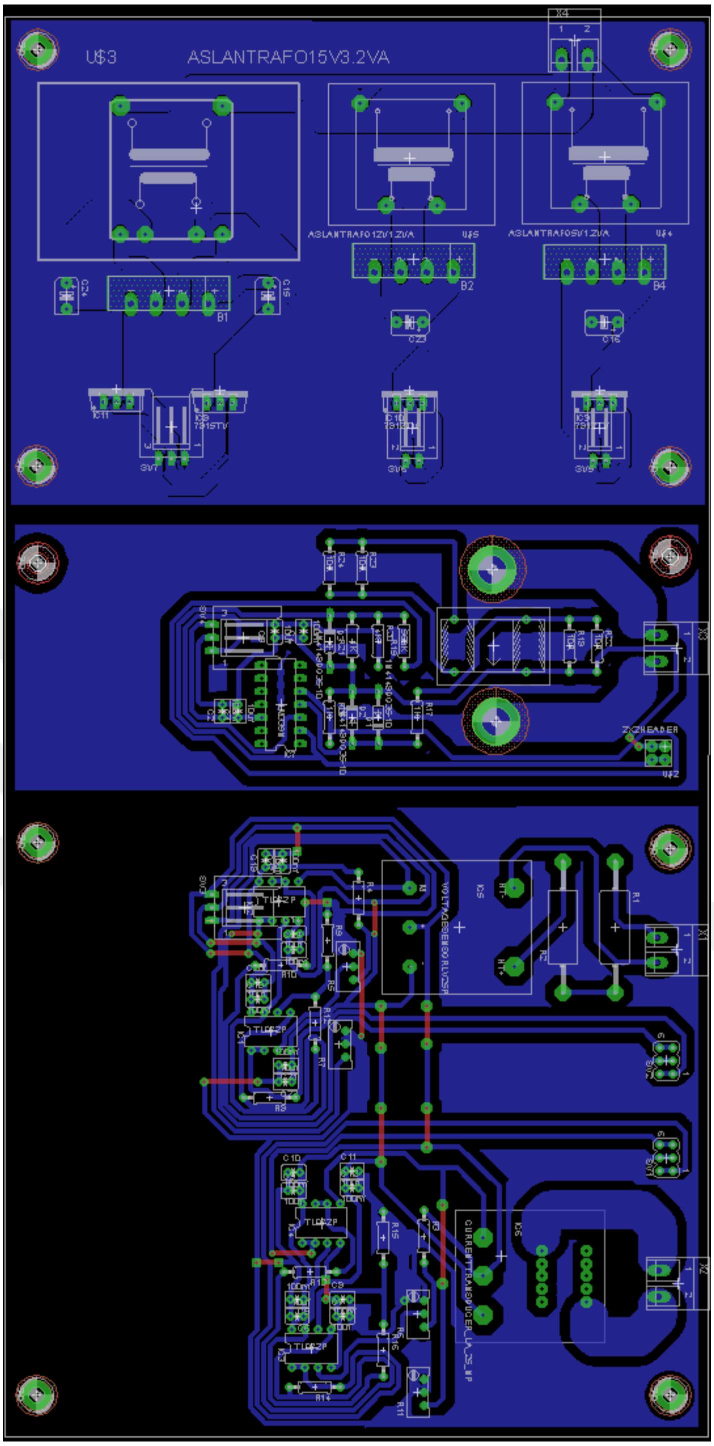

Figure A1.7 Combined zero crossing, power supply and measurement circuits

Schematic drawing of this circuit is in sensor+zero_crossing+power(11.09.2017).sch file and board drawing of it is in sensor+zero_crossing+power(11.09.2017).brd file.

1.2 Appendix B

In practical application, execution time is longer when code is loaded in flash memory. This long execution time becomes critical for fast applications. In order to eliminate any delay of microcontroller calculation, code is loaded in RAM memory. In order to achieve this,the interrupts and functions which are desired to be fast are loaded in RAM memory by the following piece of code;

#pragma CODE_SECTION(symbol, “section name”)

This code allocates a place for “symbol” in the section named “section name”. In other words, it links symbol into area “section name”.

#pragma CODE_SECTION(cpu_timer_1_isr, “ramfuncs”)

For instate, in the above code, a place is allocated for the interrupt service routine named cpu_timer_1_isr in section “ramfuncs”.